Progress in Oceanography 91 (2011) 295–311

Contents lists available at ScienceDirect

Progress in Oceanography

journal homepage: www.elsevier.com/locate/pocean

# The interannual variability of the surface eddy kinetic energy in the Labrador Sea

Hao Luo, Annalisa Bracco *, Emanuele Di Lorenzo

*School of Earth and Atmospheric Sciences, Georgia Institute of Technology, 311 Ferst Dr., Atlanta, GA 30332, United States*

ARTICLE INFO

*Article history:*
Received 17 May 2010
Received in revised form 26 January 2011
Accepted 30 January 2011
Available online 4 March 2011

ABSTRACT

The variability of the surface eddy kinetic energy (EKE) in the Labrador Sea is investigated with a suite of numerical integrations using a regional ocean model. Simulations are performed over the period 1980–2001 and are compared to satellite observations over the last 9 years. The surface EKE pattern in the basin is dominated by a region along the West coast of Greenland where eddies, mainly anticyclonic, are formed by instability of the main currents flowing over the continental slope, consistent with previous idealized results. Here the interannual changes are linked to the shear of the incoming boundary current system imposed as boundary condition to the model domain. The highly variable strength of the East Greenland current at the northeast boundary, derived from the Simple Ocean Data Assimilation (SODA) reanalysis, strongly influences the vortex formation.

In the center of the Labrador Sea, where deep convection occurs, a statistically significant portion of the modeled interannual surface EKE variability is correlated with the local atmospheric forcing, and both heat and wind fluxes play an important role and can be adopted as predictors at a lag of 2–3 months. The Arctic Oscillation index can also be used as a remote indicator of the atmospheric fluxes, but with lower skill than local measurements. In contrast the North Atlantic Oscillation index does not correlate significantly with the surface EKE at intraseasonal and interannual scales. The analysis of altimeter data over the 1993–2001 supports the existence of this asymmetry between the regime locally forced by the atmosphere in the central basin, and the regime remotely forced by the incoming boundary current along the west Greenland coast. Those results have important implications for monitoring and predicting the surface eddy kinetic energy variability in the Labrador Sea.



## 1. Introduction

Understanding the physical mechanisms that regulate the variability in the Labrador Sea circulation is central to monitoring and predicting the contribution of this basin to the Atlantic Meridional Overturning Circulation (AMOC). Wintertime deep convection there forms a dense water mass, the Labrador Sea Water (LSW), which spreads across the northwest Atlantic (Talley and McCartney, 1982) at mid-depths. While deep convection is often idealized as being predominantly driven by variations in local surface buoyancy loss, with the role of ocean dynamics being limited to gyre-scale "preconditioning", recent work has shown an active influence of mesoscale dynamics in the Labrador Sea. Observations from current meter moorings and satellite altimetry have shown the importance of long-lived coherent eddies of boundary current origin to the heat balance of the gyre interior (Lilly et al., 2003). These eddies, termed "Irminger Rings" for the warm-water boundary current they originate from, have been identified by subsequent modeling (Katsman et al., 2004; Chanut et al., 2008) and observational (Straneo, 2006; Hátún et al., 2007) studies as a major mechanism of heat and possibly freshwater flux from the boundary current to the interior. Their generation is triggered by the sudden change of the topographic slope that south of Cape Desolation becomes very steep (Fig. 1a; see also Bracco et al. (2008), their Fig. 1) and their size, determined by the topography, exceeds the Rossby deformation radius (Bracco et al., 2008). The nature of the instability mechanism itself is still a matter of debate, in particular whether the instability is controlled by surface forcing or by vertical shear at depth (Eden and Böning, 2002; Katsman et al., 2004; Bracco et al., 2008). The Irminger Rings and their associated heat transport exhibit interannual variability (Lilly et al., 2003; Rykova et al., 2009) and idealized models show that the topographic instability is sensitive to the speed of the boundary current system (Bracco and Pedlosky, 2003), which in turn may be related to the strength of the subpolar gyre and to the inflow from the Arctic via the East Greenland Current. As a result, the large interannual variations that have been observed may be independent of changes in local atmospheric forcing (Lilly et al., 2003; Brandt et al., 2004). Another main restratification mechanism is the baroclinic instability of the boundary current that occurs around the periphery of the Labrador Sea (Spall, 2004; Straneo, 2006). This instability mechanism also generates eddies with a surface signature, smaller size

* Corresponding author.
*E-mail address:* abracco@gatech.edu (A. Bracco).

0079-6611/$ - see front matter © 2011 Elsevier Ltd. All rights reserved.
doi:10.1016/j.pocean.2011.01.006

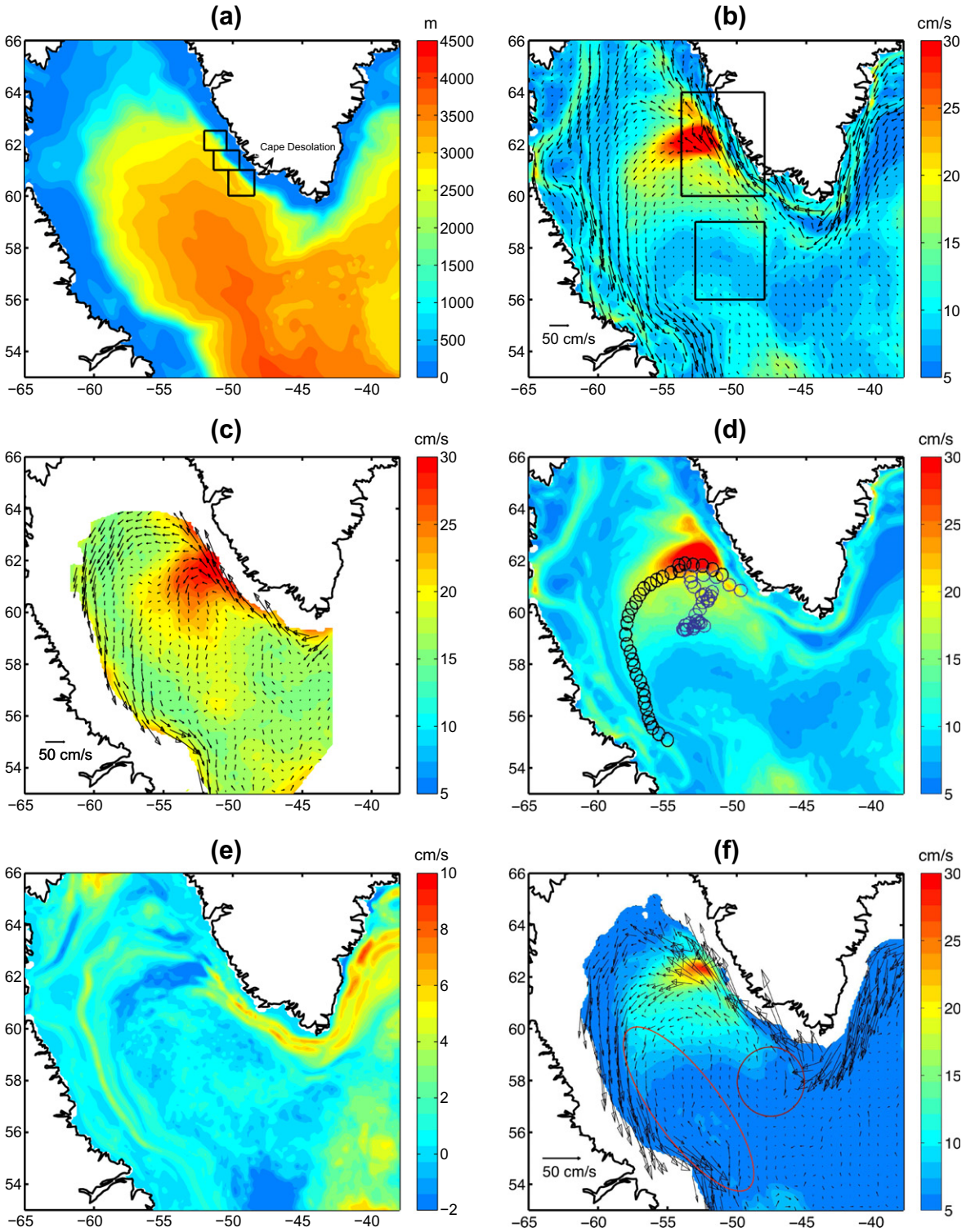


**Fig. 1.** (a) Model bathymetry. The three boxes along the West Greenland coast indicate the locations where the original ETOPO2 data are used. Cape Desolation is also indicated. (b) Annual mean distribution of surface EKE cast as a speed $V_{EKE} = (2EKE)^{1/2}$ with superimposed the horizontal velocity mean flow for the MF ensemble. The location of the WGC and CLS boxes following Brandt et al. (2004) is also indicated (see text for details). (c) Same as panel b but for TOPEX/Poseidon altimetry data over the period 1994–2000. (d) Map of $V_{EKE}$ for the MF ensemble with superimposed the trajectories of two Irminger Rings formed along the West Greenland coast and indicative of the preferred pathways for the modeled eddies. (e) Map of $V_{EKE}$ difference between $MF_{BC}$ and MF integrations. (f) Annual mean distribution of $V_{EKE}$ at 700 m depth with superimposed the horizontal velocity mean flow in MF ensemble. All model maps are averaged over the period 1980–2001 and over the two ensemble members.

(determined by the Rossby deformation radius of the basin which is about 13 km) and of somewhat different properties and shorter lifespan than the Irminger Rings (Eden and Böning, 2002; Chanut et al., 2008). Although the distribution of fluxes between these two pathways is a subject of ongoing research (Lilly et al., 2003; Katsman et al., 2004; Straneo, 2006; Chanut et al., 2008), there is general agreement that both mechanisms are important. Finally, the convective patch itself may be capable of generating 'local'

eddies without undergoing preconditioning as demonstrated by numerical studies of open ocean deep convection (Jones and Marshall, 1997; Marshall and Schott, 1999). This last possibility is supported by the recent analysis of profiling ARGO float data in combination with satellite and in situ observations by Yashayaev and Loder (2009) relative to the winter 2007–08, and by Våge et al. (2009)for the winters of 2005–06, 2006–07 and 2007–08. The onset of strong deep convection in the winter of 2007–08 does not appear as directly related to the eddy activity in the basin, but results from surface heat loss and stronger atmospheric cooling.

A better knowledge of the dynamical processes regulating the surface eddy kinetic energy (EKE) variability in the Labrador Sea will help predicting how tracer (temperature and salinity) exchanges between inshore and offshore waters respond to changes in the atmosphere and ocean states. Those changes may relate to variability in the local atmospheric fluxes, possibly linked to the North Atlantic Oscillation (NAO) (Dickson et al., 1996) or the Arctic Oscillation (AO) (Thompson and Wallace, 1998), to freshening due to ice melting, to warming in association with global climate change, and to the state of the subpolar gyre itself (Hátún et al., 2005).

In this paper, with a modeling study, we investigate the sources of surface EKE variability focusing on the central part of the basin and on the West Greenland current region. Using a regional ocean model run at 7.5 km resolution and forced by realistic atmospheric fluxes and climatological or monthly varying boundary conditions we study the sensitivity of EKE generation to external (atmospheric) and internal (oceanic, i.e. boundary conditions) forcing, while an ensemble of integrations forced only by the seasonal cycle (i.e. with climatological atmospheric and oceanic forcings) quantifies the levels of intrinsic variability. An analysis of satellite altimetry over a 9-year time period, from January 1993 to December 2001 (Brandt et al., 2004) is used to compare the variability of the modeled and observed eddy kinetic energy fields.

The material presented is organized as follows. Section 2 describes the model experiments and the domain used for this study. Section 3 discusses the mean circulation in the Labrador Sea and the eddy field characteristics. Section 4 focuses on the interannual modulations of the surface eddy kinetic energy in the three ensembles performed, with a comparison between the simulated EKE variability and the satellite observations. A summary is provided in Section 5.

## 2. Model description and configuration

The Regional Ocean Modeling System (ROMS) (Shchepetkin and Mc Williams, 2003, 2005) is used here to investigate the internal and forced eddy variability in the Labrador Sea. ROMS is a free-surface, hydrostatic, primitive equation ocean model widely used for a range of applications (Haidvogel et al., 2000; Malanotte-Rizzoli et al., 2000; Combes and Lorenzo, 2007). In ROMS, the hydrostatic primitive equations are discretized over variable topography using stretched, terrain-following coordinates in the vertical (Song and Haidvogel, 1994) and evaluated using boundary-fitted, orthogonal curvilinear coordinates on a staggered Arakawa C-grid in the horizontal. The vertical coordinate system allows for a better representation of the interactions between the flow and the bottom topography compared to the traditional height coordinate. This feature is particularly important for representing the dynamics along the west coast of Greenland. A nonlocal closure scheme is implemented for the vertical mixing parameterization based on the K-profile (KPP) boundary layer formulation (Large et al., 1994). A convective adjustment scheme for interior mixing is also activated (the LMD-KPP closure). The equations are solved using a split-explicit time-stepping scheme, which allows the separation of the barotropic and baroclinic components of the momentum equations with internal and external time steps. The terrain-following coordinates and closure schemes make ROMS an ideal tool for studying an unstable current system in the presence of topographic effects and vertical convection.

The model domain extends northward from 51°N to 66°N and westward from 35°W to 65°W. The spatial resolution is 7.5 km in the zonal and meridional directions with 30 levels in the vertical, eight of which are concentrated in the first 300 m of the water column. Although the model resolution is barely above the Rossby radius of deformation in the Labrador Sea, the model captures a large amount of the eddy variability and all three kinds of eddies described in the Introduction are present. Open boundaries are used in the east, south and north sides of the domain. Higher horizontal resolution (5 km) has been achieved in a 10-year long run in a set-up comparable to CLIM (see below for a description of the CLIM configuration) but the time-stepping required once variable atmospheric forcing is implemented decreases to less than 100 s, making the ensemble strategy implemented here impractically long. A modified radiation boundary condition (Marchesiello et al., 2001) together with nudging to climatological or monthly varying variables from Simple Ocean Data Assimilation (SODA) (Carton and Giese, 2008) is used along the open boundaries of the model domain.

The model bathymetry is derived from Sandwell and Smith (1997). In order to reduce the errors caused by the large pressure gradient of the bathymetry (Mellor et al., 1994), a smooth logarithmic interpolation, described in Penven et al. (2008), is applied everywhere except for a limited region around Cape Desolation where the original details of Sandwell and Smith (1997) are retained (Fig. 1a). Indeed, the topographic details near Cape Desolation control the boundary current meandering and the subsequent shedding of the eddies (Eden and Böning, 2002; Katsman et al., 2004; Bracco et al., 2008). Bracco et al. (2008) with their idealized experiments have shown that in the West Greenland Current region the eddy generation is due to localized instability controlled by the continental slope and that the supercriticality emerges from a steepening and subsequent flattening of the topographic slope. We have found that in ROMS any smoothing, even minimal, of the topography along the West Greenland coast reduces the extension of the supercritical region, in agreement with the sensitivity study in Bracco and Pedlosky (2003), causing a significant reduction of EKE in the proximity of Cape Desolation and the appearance of a secondary peak further north (see Appendix, Fig. A1). By retaining the details of the topography along the western side of Greenland, the model is able to better represent the observed eddy activities originated by the localized instability. We have verified that the bottom velocities along the west coast of Greenland are not significantly affected by spurious pressure gradients whenever the original details of the bathymetry are preserved close to Cape Desolation.

A first integration, CLIM in the following, is forced by monthly climatology computed over the period 1980–2001 from NCEP/NCAR reanalysis (Kalnay et al., 1996). The NCEP/NCAR monthly means data used in this project can be found at http://www.esrl.noaa.gov/psd/data/gridded/data.ncep.reanalysis.html. The NCEP/NCAR surface heat fluxes are corrected, in all runs, using NOAA extended SST (Smith and Reynolds, 2004) available at http://www.ncdc.noaa.gov/oa/climate/research/sst/ersstv3.php at a resolution of $2^\circ \times 2^\circ$. This correction, with timescale of 1 month, is done to avoid long-term drifts in the SST climatology associated with errors in the NCEP surface fluxes (Josey, 2001) and it is standard practice in the regional modeling community. More formally, the heat fluxes forcing the model ocean surface, $Q_{Mod}$, are calculated according to

$$Q_{Mod} = Q_{Ncep} + dQ_{Mod}/dSST_{Mod} \times [SST_{Mod} - SST_{NOAA}]. \quad (1)$$

In CLIM the monthly NOAA SST climatology computed over 1980–2001 is used in the correction term.

SODA reanalysis (available at http://iridl.ldeo.columbia.edu/SOURCES/.CARTON-GIESE/.SODA/.v2p0p2-4/) is used for the boundary conditions: A monthly oceanic climatology for temperature, salinity and geostrophic velocity is calculated over the 1980–2001 time interval and nudged at the open boundaries through the water column using the modified radiation condition described in Marchesiello et al. (2001). The model is spun-up from SODA climatology and after a stationary state has been reached one member, 50-year long, is considered. Therefore in CLIM both atmospheric forcing and oceanic boundary conditions are climatological and the ocean stratification in the Labrador Sea changes only with the seasonal cycle.

A second ensemble, MF (for Monthly Forcing), differs from CLIM in using as atmospheric forcing fields NCEP monthly varying winds and heat fluxes, corrected using monthly varying NOAA SSTs. MF includes two members, initialized from the CLIM solution and forced by the NCEP monthly surface fields starting in January 1975 and in January 1976, respectively. In the analysis we discard the first 5 and 4 years, respectively, and we consider only the common period 1980–2001. Two further runs have been forced by monthly varying winds and climatological heat fluxes ($MF_{Wind}$), and by climatological wind stresses and monthly varying heat fluxes ($MF_{Heat}$) to further separate their respective contributions.

A third ensemble of two members, $MF_{BC}$ (Monthly Forcing including Boundary Conditions), is nudged to monthly varying boundary conditions from SODA at the boundaries, to investigate how the interannual variability in the incoming boundary current system modifies the circulation. In $MF_{BC}$ the ocean stratification in the basin changes on a monthly base following SODA. These integrations are also initialized with CLIM fields and are forced by monthly varying atmospheric fluxes of heat and momentum as in MF and oceanic boundary conditions starting in 1975 and 1976. Again we consider the 1980–2001 period. Unfortunately the paucity of in situ data seriously undermines the confidence of the ocean reanalysis. The incoming current system derived from SODA is characterized by large interannual variations in the first 200 m of the water column and localized at the north-east corner of the domain. We verified the reliability of those variations using two other reanalysis datasets, the JRA-25 reanalysis by the Japan Meteorological Agency (Masuda et al., 2009) and the ECMWF System 3 ocean reanalysis (Balmaseda et al., 2007): We did not find any statistically significant correlation between the three time-series for the incoming surface current over the 1980–2001 time-frame after removing the seasonal cycle (even if some similarity can be found on shorter periods and they share an analogous variance). Analyzing the source of variability at the boundary of our model domain is a complicated task and beyond the scope of this paper. The area is indeed affected by Arctic discharge, gyre oscillations and intense atmospheric fluxes. For the purpose of this work, however, the reader should bear in mind that results from the $MF_{BC}$ ensemble may be biased by the reliability of the interannual changes in the ocean reanalysis boundary conditions.

## 3. Mean circulation and eddy field

### 3.1. Definition of EKE and processing of model output and satellite data

In the following we will compare eddy kinetic energy maps and time series calculated from the model output and satellite data. The model output consists of 3-day averages of the horizontal velocity components, $u_{Tot}$ and $v_{Tot}$, computed automatically during the integrations (i.e. averaging fields at each 300-s time step), so time aliasing is never an issue. The EKE is then calculated, after subtracting the total mean to obtain $u$ and $v$, as $EKE = [(u^2 + v^2)]/2$. For the time-series, EKE monthly averages are then subtracted to remove the seasonal cycle. Sea surface high anomaly maps are calculated removing the seasonal cycle, but grouped into seasons. This procedure retains contributions from interannual velocity fluctuations and not only from the mesoscale (Penduff et al., 2004), but allows us to directly compare the model results with the time-series in Brandt et al. (2004) and the EKE maps published in earlier studies (i.e. Lilly et al., 2003; Chanut et al., 2008). The satellite data consist of TOPEX/Poseidon, with 127 ascending/descending tracks during a 9.92 day period and of ERS-2, with 501 tracks during a period of 35 days. The along-track grid size for TOPEX/Poseidon data is between 5.7 and 6.2 km and for ERS-2 is 6.6 km. The procedure utilized to remove high noise level inherent to sea level anomalies induced by the sea surface roughness due to wind waves and/or swell retrieved from TOPEX/Poseidon and ERS-2 is outlined in detail in Brandt et al. (2004). The data are mapped into a $0.2^\circ \times 0.2^\circ$ horizontal grid and after subtracting the total mean, the velocity data are 2 day low-pass filtered to remove the tidal signal and grouped into monthly averages. The *EKE* is then calculated as for the model data as $EKE = [(u^2 + v^2)]/2$. Monthly averages are then removed, as for the model output. The altimeter time-series provide therefore useful information on regional, seasonal and interannual aspects of the surface eddy field, and on those we will focus our comparisons, but they do not allow detection of very small and weak eddies. The altimetric EKE has been compared in Brandt et al. (2004) to the time-series computed from moored observations and found in good agreement after the correction for the sea surface roughness was applied, in particular in the Central Labrador Sea.

### 3.2. Modeled mean circulation

The modeled surface annual mean circulation is mainly cyclonic with swift currents around the basin. The maximum transport in the basin is 42 Sv (1 Sv = $10^6$ m$^3$ s$^{-1}$), in good agreement with the estimate by Reynaud et al. (1995), Pickart et al. (2002), Fisher et al. (2004) and the more recent, still unpublished estimate by M. Hall, D. Torres and I. Yashayaev (American Geophysical Union, Fall Meeting 2010, abstract number OS41C-1572). Fig. 1b shows a map of the annual mean distribution of surface EKE cast as a speed $V_{EKE} = (2EKE)^{1/2}$ for the MF ensemble and should be compared with the EKE map computed from TOPEX/Poseidon satellite altimeter data over the 1994–2000 period (Fig. 1c, data courtesy of J. Lilly; see also Lilly et al. 2003; their Fig. 24). Superimposed on the modeled EKE map is the mean horizontal velocity field averaged over 22 years and over the two runs in the MF ensemble (no significant differences are found if only one integration is used instead).

Overall, the eddy activity in the Labrador Sea is moderate over most of the basin in both the model and observations. An energy maximum extends from the West Greenland coast into the interior of the Labrador Sea near 61–62°N, and is associated with the separation from the coastline of the West Greenland Current (WGC) that divides in two branches near Cape Desolation following the 2000 and 3000 m isobaths (Cuny et al., 2002). Here the maximum $V_{EKE}$ reaches values of 32 cm/s, in agreement with the satellite data. The model likely underestimates significantly the EKE at the southern tip of Greenland, in the so-called Greenland tip jet (Pickart et al., 2003). Incidentally, both in this region and along the western side of the domain EKE values about twice as large have been found in a short 6-year run forced by daily winds derived from QSCAT satellite measurements and daily NCEP/NCAR heat fluxes, and not discussed in this work. This EKE increase is due to a slight increase in number and a significant increase in strength of the eddies and it is indicative of an important role for strong, intermittent

wind events in those locations, in agreement with the work by Våge et al. (2008).

In the more quiescent regions the model EKE underestimates the altimetry data and the amplitude of the signal is about half of the observed one, but it is in agreement with other modeling results (Eden and Böning, 2002; Chanut et al., 2008). This discrepancy may be partially due to the high noise level in the satellite observations whenever EKE values are very low (Lilly, personal communications). Again, imposing 6-hourly wind forcing improves the model representation of the EKE levels. The mean velocity field is also indicative of two preferred paths of separation of the West Greenland Current into the interior. Those paths will be followed by the rings formed along the Greenland coast to move into the basin interior (Fig. 1d; see later in this section).

Similar EKE maps are obtained in the other experiments; differences are significant only between $MF_{BC}$ and MF (Fig. 1e). Monthly varying boundary conditions induce a variability in the surface EKE along the eastern side of Greenland that is twice as strong as MF. In $MF_{BC}$ EKE levels are approximately 30% and 15% higher than in MF in the boundary current system along the western side of Greenland and in the Central Labrador Sea, respectively. The surface EKE increase results from a higher degree of instability of the boundary current system around Greenland, as we will discuss later, and it induces a modeled Irminger Ring population that is more intense and longer living in $MF_{BC}$ than in MF.

The mean horizontal velocity field at 700 m, displayed by arrows in Fig. 1f, shows a series of closed cyclonic recirculations or counter flows in the Labrador Sea interior, in agreement with the analysis by Lavender et al. (2000). The modeled cells, however, are characterized by weaker velocities than the ones deduced from subsurface floats. Pickart et al. (2002) suggested that those cells may contribute to the localization of deep convection in the southwest of the basin. The EKE distribution at 700 m displays a maximum located near Cape Desolation, in correspondence to the surface one, and low levels elsewhere in the basin. At 700 m monthly varying boundary conditions do not differ significantly from their monthly climatological values and differences between the various integrations are negligible (not shown).

In Fig. 2a the seasonal maps of sea surface height (SSH) variance are shown averaged over the two MF ensemble members (again, differences between members are negligible). The model reproduces the seasonal cycle quite accurately over most of the basin (see Prater (2002) for the corresponding figure derived from satellite measurements). The SSH variance is higher in winter along the basin boundaries and north of Cape Desolation, remains high in spring relative to the Irminger Rings formation and propagation, and is reduced in summer and fall.

Panels b and c provide a quantitative assessment of the accuracy of the modeled seasonal cycle of EKE over two boxes identified as WGC and CLS (Central Labrador Sea) following Brandt et al. (2004) for both MF and $MF_{BC}$ runs. The WGC box is defined over (60°N–64°N and 48°W–54°W) and the CLS in the (56°N–59°N and 48°W–53°W) region (see Fig. 1a). The observations used for comparison are constructed from TOPEX/Poseidon data over the period 1993–1997 and merged TOPEX/Poseidon and ERS data for the period 1997–2001 (time-series courtesy of F. Schott and published in Brandt et al. (2004)). The EKE signal, averaged over the whole boxes, is about 20–30% stronger in the satellite data than in the model (note the different scale used for the data – left $y$-axis, in black – and for the model results – right $y$-axis, in blue for both runs). Focusing on the annual cycle, the model slightly overestimates the production of Irminger Rings in the WGC region in spring and in particularly in March and April and underestimates it in January/February, with an overall shift of the seasonal cycle of about 1 month (Fig. 2b). When varying boundary conditions are implemented the amplitude of the modeled signal is stronger and $MF_{BC}$ runs compare better with the observations. Notwithstanding the amplitude, the seasonal cycle of the EKE anomalies is very well represented in the CLS region in both ensembles (Fig. 2c), with a EKE maximum in April and a secondary peak in fall corresponding to a larger production of eddies in those seasons (see also the relative vorticity movie available as Supplementary material).

Fig. 3 shows the annual mean stratification profile for potential temperature along the AR7W section between Hamilton Bank, on the Labrador coast, and Cape Desolation on the Greenland coast in the MF runs, averaged over the 1980–2001 period. The reader is referred to Yashayaev (2007) (his Fig. 3) for the equivalent section from the hydrographic dataset of the Bedford Institute of Oceanography in 1994 and 2005 and to Chanut et al. (2008) for an average over all sections available (their Fig. 7a, data courtesy of I. Yashayaev). Single snapshots at different times of the year have been presented in various works (Pickart et al., 2002; Cuny et al., 2002; Lilly et al., 2003; Yashayaev and Loder, 2009). Near the surface, the West Greenland Current, characterized by cool waters ($T \sim 2$°C and $T \sim 1$ °C in the model and observations, respectively) retains its properties while flowing around the basin to become the Labrador Current (LC). Both currents are confined to the shelf break in the model runs. The warm Irminger Current is found immediately off the shelf, with temperatures reaching 6 °C in its core. Its signature is also evident on the Labrador side. Part of its heat content is lost to the interior while moving around the basin through mixing associated with the formation of coherent eddies and with atmospheric cooling. At mid-depth, between 1000 and 2200 m, we find the Labrador Sea Water (LSW), formed through convective activity. Below it, the Northeast Atlantic Deep Water (NEADW) and Denmark Strait Overflow Water (DSOW) occupy the remainder of the water column. The model represents the vertical structure of temperature and density in the Labrador Sea reasonably well. The interior, however, is too warm, but this is a common problem in most ocean circulation model outputs (Treguier et al., 2005), including SODA that is providing the boundary conditions, and the vertical stratification is, consequently, weaker than observed. Additionally, at the Greenland coast the surface layer of cold water protrudes unrealistically along the shelf, and the warm Irminger current is not as firmly attached to the sloping bottom as observed (Yashayaev and Loder, 2009).

### 3.3. Eddy field characteristics

The Irminger Rings, formed along the coast of Greenland, are the major contributors to the eddy kinetic energy in both the model and observations. The Irminger Ring generation appears as a highly localized ejection of boundary current waters (Prater, 2002; Rykova et al., 2009) associated with a steepening and subsequent flattening of the topographic slope. A movie of the relative vorticity at the surface, available as Supplementary material, shows that the formation of the eddies is a compound process involving generation of vorticity by localized baroclinic instability along the coast of Greenland around 61°N, where the 3000 m isobath approaches the continental slope, followed, in most cases, by a northward displacement of anticyclonic vorticity along the coast, and finally by detachment of single anticyclones or dipoles around 62°N, independently of the integration considered. Eden and Böning (2002) suggested that seasonal variation in the barotropic strength of the West Greenland Current was the determining factor for the seasonal changes in eddy kinetic energy of the region. Katsman et al. (2004) instead found that the instability process is mixed, with barotropic energy conversion prevailing at the surface and baroclinic conversion dominating at depth. Additionally, the annual cycle of heat loss in the upper water column was found to be an important contributor to the seasonal signal in the eddy

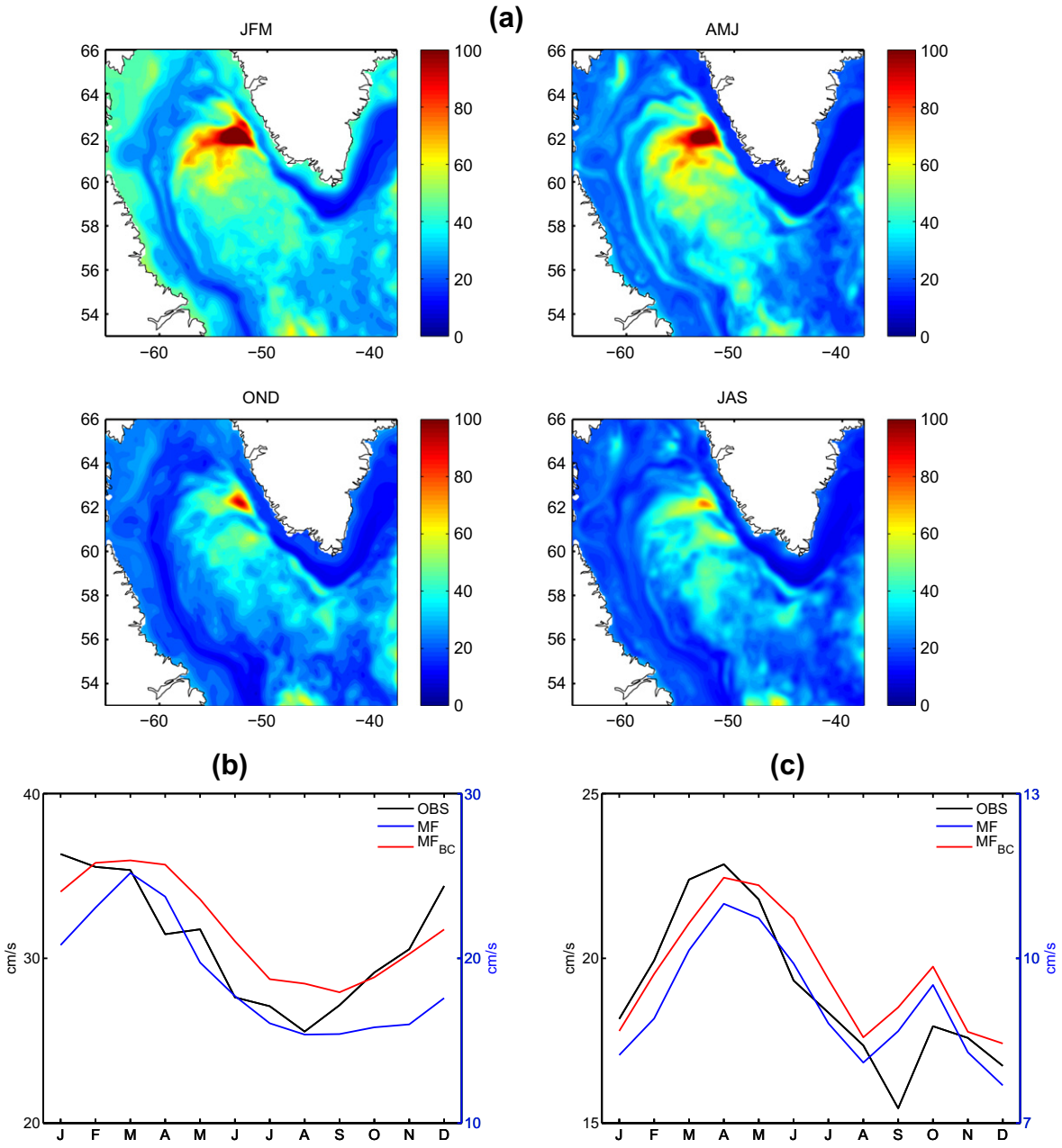


**Fig. 2.** (a) Seasonal maps of SSH variance for the MF ensemble, calculated over the period 1980–2001; (b and c) EKE seasonal cycle in the WGC and CLS regions, respectively, for TOPEX/Poseidon data averaged over 1993–2001 (black line), and for the MF (blue) and $MF_{BC}$ (red) ensembles averaged over 1980–2001. A different scale is used for the observations (left *y*-axis, in black) and the model runs (right *y*-axis, in blue for both MF and $MF_{BC}$). No significant changes are found if the model analysis is limited to 1993–2001. (For interpretation of the references to colour in this figure legend, the reader is referred to the web version of this article.)

generation. To examine the generation mechanism in more detail, Bracco et al. (2008), following earlier work (Bracco and Pedlosky, 2003), analyzed a three-layer quasigeostrophic channel model with idealized topography. The generation of the eddies was found to arise from a local baroclinic instability of the bottom flow at the upstream edge of the topographic flattening. Downstream energy fluxes reflect the barotropization of the initially baroclinic, bottom-trapped disturbances as they grow to finite amplitude until they reach the downstream step and are injected into the interior. The net result is an eddy-driven flux of water from the boundary current into the interior of the basin which involves the entire water column. A similar scenario was described by the laboratory modeling of Wolfe and Cenedese (2006), who examined generation of vortices by a bottomed-trapped current flowing over a topographic gap. Those idealized numerical or laboratory experiments are relevant to the MF integrations, where climatological boundary conditions are used and the current system varies only according to the seasonal cycle. Indeed we find the generation mechanism described in Bracco et al. (2008) at work in the MF ensemble and in the $MF_{Wind}$ and $MF_{Heat}$ runs.

In the mechanism proposed by Bracco et al. (2008) the strength of the bottom current is directly linked to the strength of the instability, and this is confirmed in our MF experiments, at least at interannual scales. Fig. 4a displays for one of the MF runs the EKE anomalies in the WGC region calculated over the top 50 m of the water column and the EKE anomalies at a north–south section located at 45°W and extending from 59° to 59.5°N (i.e., just around the tip of Greenland) calculated over a layer extending from 310 m

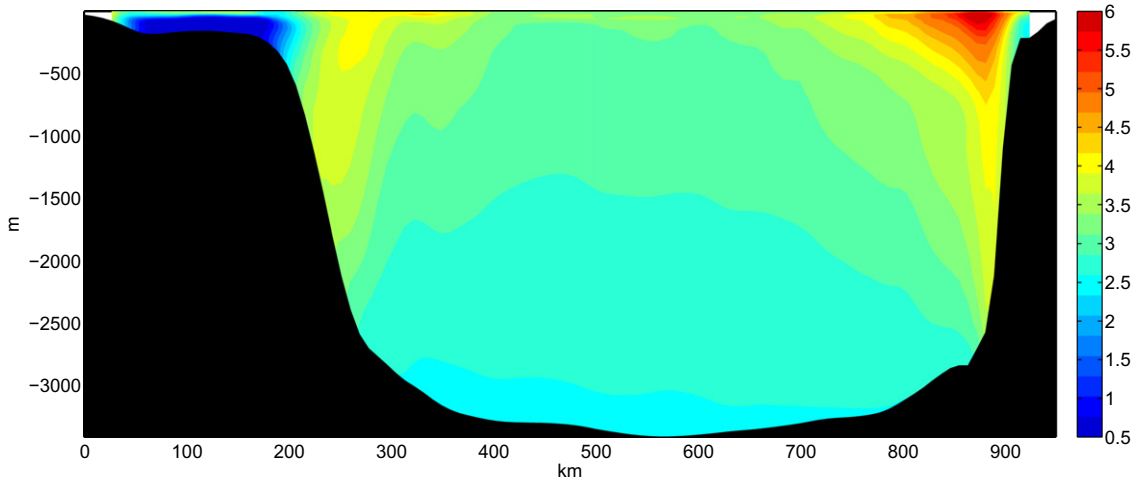


**Fig. 3.** Annual mean stratification profile of potential temperature along the AR7W section, averaged over the 1980–2001 period.

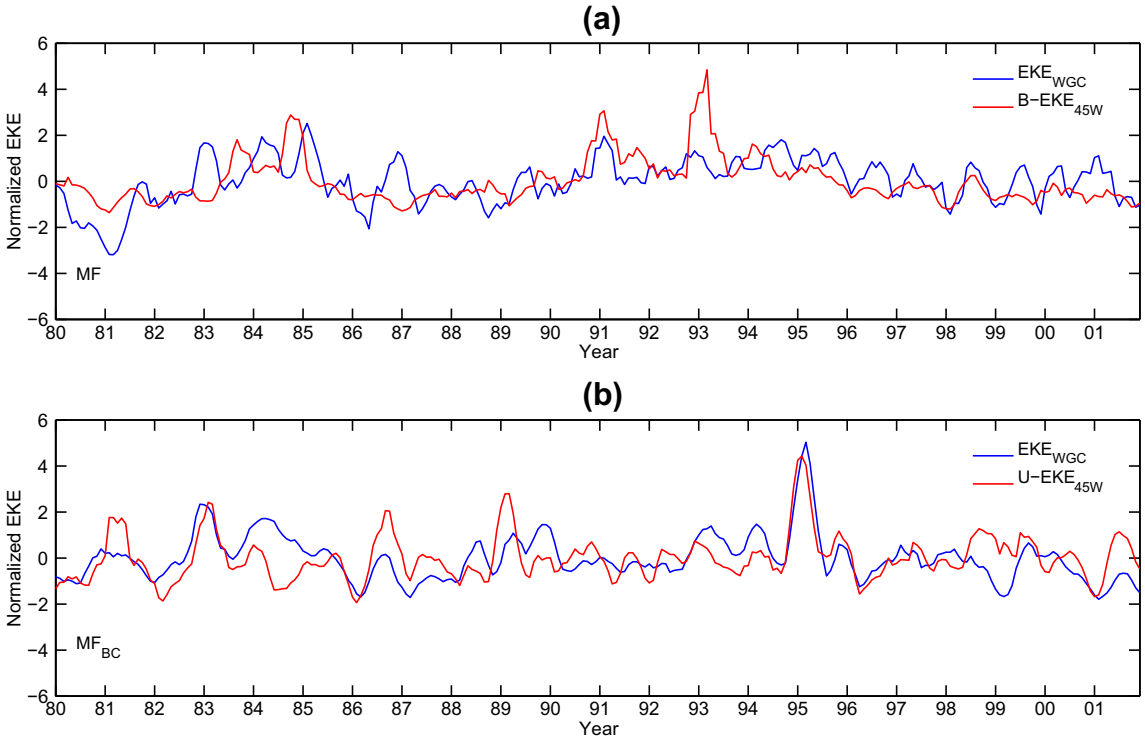


**Fig. 4.** Time-series of EKE anomalies in the West Greenland Current region shown in Fig. 1a (blue) and of (a) bottom current strength at a section located at 45°W and 59–59.5°N (red) for one of MF ensemble members. (b) Upper current strength at a section located at 45°W and 59–59.5°N (red) for one of $MF_{BC}$ ensemble members. (For interpretation of the references to colour in this figure legend, the reader is referred to the web version of this article.)

to 150 m above the bottom and therefore representative of the strength of the bottom current. The section is far from the WGC box, and is characterized by a predominantly longitudinal flow. The variance of the two time-series has been normalized to unity, for clarity in the visualization, and the time-series are 99% statistically significantly correlated whenever a 5-month (11-month) running mean is used, with correlation coefficient $cc = 0.45 \pm 0.06$ ($cc = 0.66 \pm 0.06$). No statistically significant correlations are found between the surface EKE anomalies at the same section (45°W) and the surface EKE in the WGC region.[1] In the MF ensemble we implemented climatological boundary conditions and the interannual variability in the bottom current strength is due to internal oceanic processes linked to episodes of vortex formation along the east side of Greenland (not shown).

In the $MF_{BC}$ case, on the other hand, the level of realism is augmented by the introduction of monthly varying boundary conditions, and the shear in the boundary current system is strongly affected by the time dependence of the upper flow. The variability of the incoming upper current is determined by SODA boundary conditions and it affects the interannual variability of the eddy formation in correspondence of the topographic step at 61°N. A detailed description of the process at play can be found in Flierl and Pedlosky (2007). The generation mechanism is still by local baroclinic instability over the topographic step, and the Rings have analogous diameter – determined by the topography – and vertical

[1] In this work the correlation for the MF and $MF_{BC}$ ensembles results from averaging the coefficient obtained for each of the two members, and the error expresses the intra-ensemble variability. The statistical significance of the correlations is established using a *t*-test when not specified otherwise.

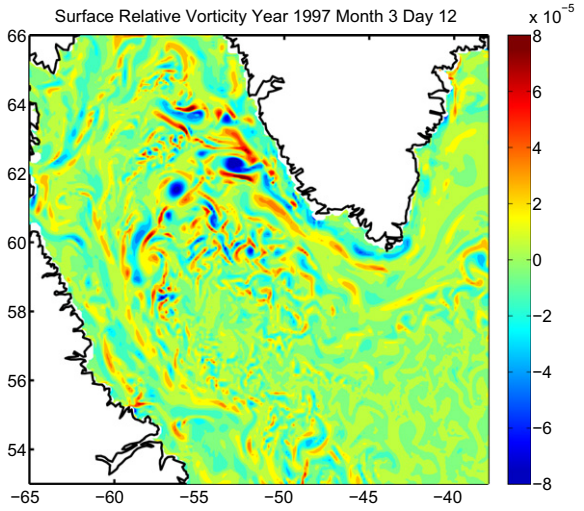


**Fig. 5.** Snapshot of surface relative vorticity on March 12, 1997 for one member of the MF ensemble.

extension – from the surface to the bottom, but close to the surface they are stronger in amplitude than the ones found in the MF runs. Fig. 4b shows the EKE anomalies in the WGC region and the upper current strength calculated over a layer extending from 25 m to 100 m from the surface, again at the section at 45°W. The correlation between the two time-series is $cc = 0.53 \pm 0.05$ ($cc = 0.59 \pm 0.06$) if a 5-month (11-month) running mean is used, and it is statistically significant also on a monthly base with $cc = 0.47 \pm 0.07$. No significant correlations are found when considering the bottom current strength. We can conclude that in the Labrador Sea the incoming surface boundary current exercises a strong control on the intraseasonal and interannual variability of the WGC region.

In all runs only few anticyclones penetrates in the interior immediately after formation. About 25 Rings are formed every year, in general agreement with the estimate by Lilly et al. (2003), and their signature extends to 3000 m depth. The Rings formed in the $MF_{BC}$ runs, being more intense, are longer-lived than the ones in MF.

A snapshot of the vorticity field is shown in Fig. 5, while the two preferred paths followed by the Irminger Rings after detachment are presented in Fig. 1d. Vortices have been identified using the Okubo–Weiss parameter $OW = S^2 - \zeta^2$, where $S$ is strain and $\zeta$ is vorticity (Weiss, 1981). Petersen et al. (2006) showed that $OW$ in two-dimensional and quasigeostrophic flows is proportional to the middle eigenvalue of a tensor of velocity gradients. The same eigenvalue is used to identify coherent structures in 3-D turbulent flows but in a solution of the primitive equations, as our model runs, $OW$ represents only an approximation of the middle eigenvalue of the velocity gradient tensor. However, it still provides a clear-cut separation between vorticity-dominated regions where $OW \ll 0$ and strain-dominated regions where $OW \gg 0$ whenever divergence is small, as in our case. Vortex cores are associated with strongly negative values of $OW$ and are characterized by a spherical or quasi-spherical shape (Bracco et al., 2000). In the MF runs about 80% of the modeled Rings identified by $OW$ follow the northern path around the basin, with the remaining penetrating into the interior, but seldom reaching as south as 58°N. This is evident in Fig. 6, where we show the latitude–time diagram of the surface EKE in one of the MF and $MF_{BC}$ runs, averaged between 48° and 54°W over the 1993–2001 period, to be compared with the observed one from Brandt et al. (2004). A slightly higher percentage (about 25%) follows the interior path in $MF_{BC}$, again indicating the fundamental role played by the incoming current on the eddy

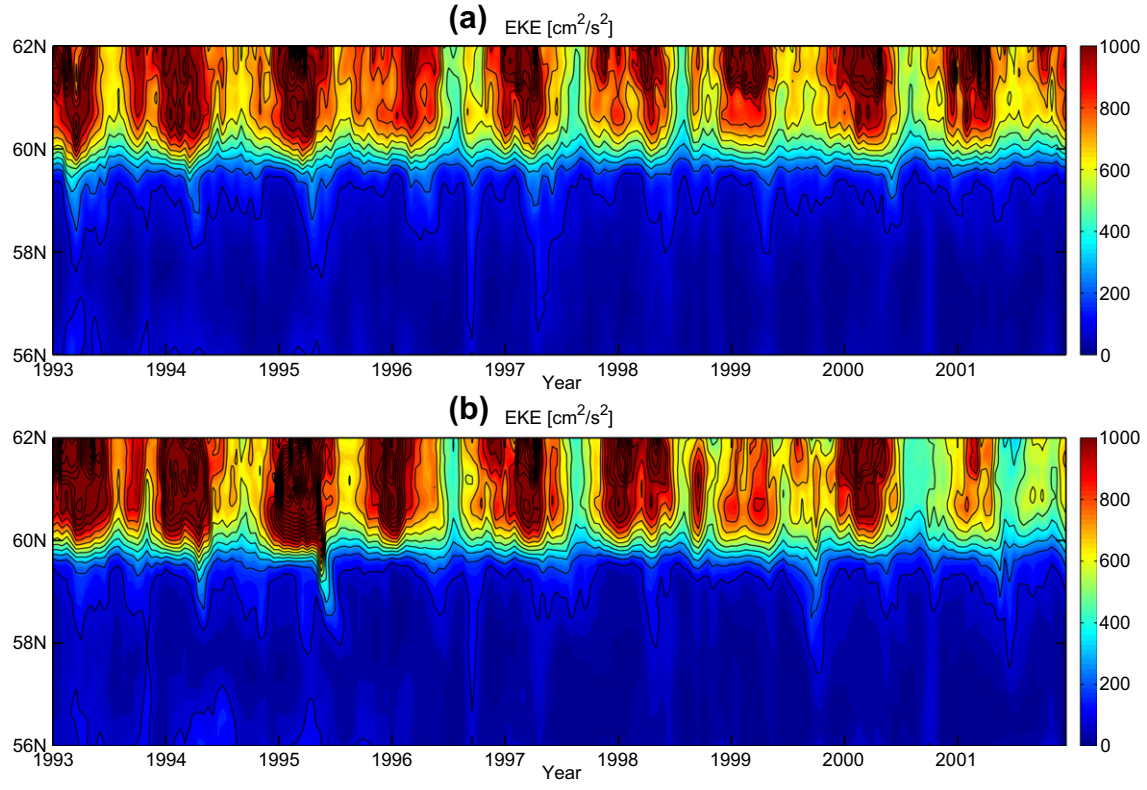


**Fig. 6.** Latitude–time diagram of the modeled EKE in the Labrador Sea averaged between 48° and 54°W for the period 1993–2001 for the MF (a) and $MF_{BC}$ (b) experiments, to be compared with the satellite data analysis in Brandt et al. (2004) (their Fig. 7).

characteristics. If their signature is followed at 50 m below the surface, the modeled Rings live 8 and 11 months on average in MF and $MF_{BC}$ integrations, respectively, but none of them survives through a second winter. Their surface signal is shorter living – rarely more than 6 months. In the observational records several Irminger Rings experience convective events over two winters and are observed in the vicinity of the OWS Bravo mooring site Lilly et al. (2003) and Rykova et al. (2009). The model therefore underestimates both the lifespan and the southern displacement of the Rings. Both problems are reported also in Chanut et al. (2008) and are likely due to the model horizontal and vertical resolution, to the representation of mixed-layer processes and to the low frequency (monthly) atmospheric forcing. The shorter CLIM integration run as test at 5 km horizontal resolution showed an improvement in the modeled eddy lifespan. The time-stepping required by such resolution with monthly varying boundary conditions, however, is of the order of 50–75 s, which is too short to allow for ensembles and multiple set-ups.

In Fig. 7 we present the barotropic ($T_4$) and baroclinic ($T_2$) conversion terms following Beckmann et al. (1994) and defined as:

$$T_2 = \frac{g}{\rho_o}\int \frac{\overline{u'\rho'}(\partial\bar{\rho}/\partial x) + \overline{v'\rho'}(\partial\bar{\rho}/\partial y)}{\partial\bar{\rho}/\partial z}\,dV \tag{2}$$

and

$$T_4 = -\int \overline{u'u'}\frac{\partial\bar{u}}{\partial x} + \overline{u'v'}\left(\frac{\partial\bar{v}}{\partial x} + \frac{\partial\bar{u}}{\partial y}\right) + \overline{v'v'}\frac{\partial\bar{v}}{\partial y}\,dV \tag{3}$$

where the overbar and the prime represent time average and deviation from the mean, respectively. $\rho$ is density, $\rho_o$ is the density reference value, $u$ and $v$ are the horizontal components of the velocity field and $g$ is the acceleration due to gravity. $T_4$ and $T_2$ are calculated for MF and $MF_{BC}$ and are vertically averaged over the whole water column (in Fig. 7) or only over 100–400 m from the surface (shown in the Appendix in Fig. A2) as in Eden and Böning (2002). The plots clearly indicates a much higher baroclinic than barotropic energy conversion in both MF and $MF_{BC}$. When the vertical integration is limited between 100 and 400 m depth we recover results comparable to Eden and Böning (2002) for the MF ensemble, with a more limited baroclinic contribution, and almost unchanged baroclinic and barotropic conversions in $MF_{BC}$. This provides another quantification of the different mechanisms of vortex formation at play in the two ensembles. In MF the instability is driven and modulated by the bottom-intensified component of the boundary current as described in Bracco et al. (2008). But if the West Greenland current is highly variable, much more than the bottom current, as in $MF_{BC}$, the background time dependence at the surface modulates the instability, as described in Flierl and Pedlosky (2007).

In the model integrations a population of eddies of smaller size of the Irminger Rings, shorter lifespan (about 3 months), extending to the bottom and predominantly anticyclonic forms around 59°N and populates the CLS region. Those eddies account for at least 80% of the simulated EKE in this area, display a different seasonality than Irminger Rings, as evinced in Fig. 2, and their formation is driven by variability in the atmospheric fluxes, as we will show in the next session. This family of eddies has been identified also in XBT sections (I. Yashayaev, personal communication), but appears to be longer living than the modeled ones. Again, the model resolution is likely responsible for the underestimation of their lifespan.

## 4. Interannual variability of the surface kinetic energy field

The extensive set of experiments performed allows us to investigate the sources of surface EKE interannual variability in Labrador Sea and to compare modeled and observed time-series for the first time in a modeling framework.

The comparison of the variability in members of the same ensemble that differ only in the initialization of the atmospheric forcing (MF), or in the initialization of the atmospheric forcing and of the monthly varying oceanic boundary conditions ($MF_{BC}$) allows for determining whether the anomalies are externally forced and with some degree of predictability, or due to intrinsic oceanic variability, uncorrelated because of the chaotic behavior of the internal instability processes, and unpredictable. The analysis of the MF and $MF_{BC}$ ensembles reveals that a large portion of the modeled EKE in the Labrador Sea is externally forced. The correlation between the EKE anomaly time-series of the two members of each ensemble, calculated over the whole basin (horizontally averaged in 53°N–66°N, 38°W–65°W) and after removing the seasonal cycle, is very high, with $cc = 0.74$ in the MF case and $cc = 0.90$ for $MF_{BC}$. This provides a first clear indication that the oceanic variability internal to the Labrador Sea basin plays a limited role and the external forcing-atmospheric in MF, atmospheric and oceanic through the monthly varying boundary conditions in $MF_{BC}$, drives the modeled anomalies. Focusing on smaller domains, $cc$ between 0.7 and 0.85 are found everywhere using monthly data, with the exception of the WGC region. In the WGC box the chaotic oceanic variability within the model domain modulates the eddy formation in the MF case and the correlation between the two members decreases to 0.43. In $MF_{BC}$ the oceanic boundary conditions common to the two members determine the variability in the vortex population, as seen in the previous section, and the correlation reaches $cc = 0.89$.

With the goal of identifying the external forcing responsible for the EKE variations, we performed the $MF_{Wind}$, $MF_{Heat}$ integrations. It is known that in the North Atlantic at interannual scales heat flux anomalies are due in large part to the momentum fluxes (Cayan, 1992; Kushnir, 1994), and that those anomalies are integrated by the mixed-layer and determine the mixed-layer temperature balance (Halliwell and Mayer, 1996). We will show that the $MF_{Wind}$ and $MF_{Heat}$ runs allow us to confirm those results and to validate the model first-order description of the mixed-layer dynamics. In Fig. 8a the monthly averaged kinetic energy over the whole domain is displayed for CLIM, one MF ensemble member, $MF_{Wind}$, $MF_{Heat}$ and one $MF_{BC}$ ensemble member over the 1993–2001 period. We confine our attention to the latter 9 years of integration in the figure for clarity purposes. The seasonal cycle dominates the EKE variability and explains about 80% of the correlations between the various time-series. Once removed, it is evident that the wind stress exerts the largest control on the modeled EKE (Fig. 8b). $MF_{Wind}$ and MF display indeed comparable interannual variation. The correlation between the two time-series is $cc = 0.77 \pm 0.06$ over the period illustrated and $cc = 0.72 \pm 0.02$ for the whole 1980–2001 record. Those values are 99% statistically significant. The $MF_{Heat}$ integration explains a smaller, but still significant fraction of the interannual signal seen in MF and the correlation between the two is $cc = 0.41 \pm 0.01$ ($cc = 0.34 \pm 0.01$ for 1980–2001). Adding time-varying boundary conditions from SODA causes the EKE to spike in certain years, as in 1995–1996, to levels that are almost twice as large as average. The $MF_{BC}$ time-series are characterized by years of intense variability in response to wind events (e.g. 1993, 1994, 1998) in agreement with the other runs, and to variations in the strength of the incoming surface boundary current (e.g. 1995, 1996, 1999, 2001) not displayed in any other time-series; its correlation with MF is $cc = 0.59 \pm 0.02$ and is 99% statistically significant.

Focusing on the WGC region, the oceanic boundary conditions influence the surface kinetic energy variability in the $MF_{BC}$ ensemble (Fig. 8c). Changes in strength of the incoming surface current at the north-east side of the domain are linked to the peaks seen in the time series for the whole domain and for the WGC region. Monthly variability in the atmospheric forcing fields contributes

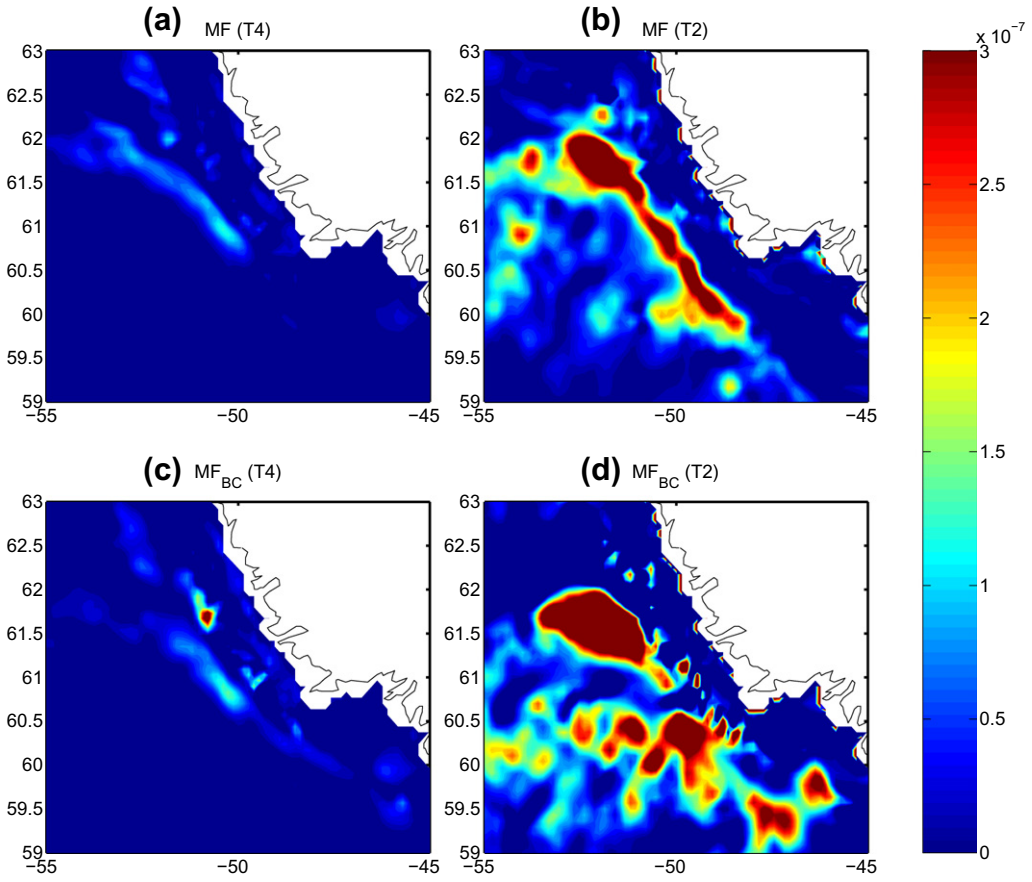


**Fig. 7.** Barotropic ($T_4$, left panels) and baroclinic ($T_2$, right panels) conversion terms vertically averaged over the whole water column and calculated for MF (top) and $MF_{BC}$ (bottom).

little in this region, and the correlation between MF and $MF_{Wind}$ ($MF_{Heat}$) after removing the seasonal cycle decreases to $cc = 0.22 \pm 0.04$ ($0.23 \pm 0.02$) and is not significant. This analysis indicates again that oceanic internal variability along the West coast of Greenland plays an important role at interannual scales whether the incoming current varies only with the seasonal cycle.

In the CLS region (Fig. 8d), on the other hand, it is evident that the atmospheric forcing is key to the modeled EKE variations: After removing the seasonal cycle the correlation between MF and $MF_{Wind}$ is $0.62 \pm 0.02$ for the whole record and $cc = 0.67 \pm 0.07$ in the 1993-2001 period, while for $MF_{Heat}$ the correlation with MF is $cc = 0.46 \pm 0.04$ in the 90s. Slightly higher values are found when the whole record is considered ($cc = 0.58 \pm 0.05$). We verified that this is associated to a larger (anti)correlation in the NCEP/NCAR reanalysis between surface winds and heat fluxes before 1992 in this particular region. The $MF_{BC}$ time-series is also modulated by the wind stress and a 99% statistically significant correlation is found between $MF_{BC}$ and $MF_{Wind}$ ($cc = 0.52 \pm 0.04$). The modeled EKE variability in the CLS box is therefore partially forced by the atmosphere and the variability in the oceanic boundary conditions affects it only moderately.

Summarizing, in the WGC box oceanic variability is important when climatological boundary conditions are implemented and little predictability is found in this area based on the atmospheric variables alone. In the $MF_{BC}$ integrations the strong interannual changes in SODA incoming current system at the north-east corner of the domain insure a higher degree of reproducibility between the two members. In the CLS region the modeled EKE appears to be externally forced to a significant extent, and the ocean internal variability within the Labrador Sea plays a minor role. Here atmospheric fluxes are the dominant forcing. The EKE for the whole basin contains contributions from both the atmospheric forcing and the incoming boundary currents, with the last being dominant only in the WGC region.

Before analyzing in more detail the potential for predictability, we validate our model results against the satellite observations comparing the EKE anomaly time-series over the common period 1993–2001 for the MF and $MF_{BC}$ ensembles. In the WGC region the time-series from all four ROMS integrations and satellite observations after removing the monthly averages are not correlated ($-0.2 < cc < 0.2$ also when a 5-month low-pass filter is used), despite the realistic representation of the seasonal cycle. Indeed if the monthly climatology is retained, the correlation between model and observed EKE exceeds 0.42 for both ensembles. In Fig. 9a we display the time-series for one of the MF and one of the $MF_{BC}$ members, and for the observations. Even if some commonality can be found at decadal scales, the interannual variability is clearly different between the two runs, with SODA boundary conditions dominating in the $MF_{BC}$ case, as evident particularly in 1995 (both $MF_{BC}$ members show the unrealistically strong peak due to the strength of the incoming current at the upper right corner of the domain found in SODA). This is not surprising in light of our analysis of the eddy generation mechanism. In MF the EKE anomalies are driven by the intrinsic variability of the bottom current, and therefore they cannot match the observations. In $MF_{BC}$ the monthly varying boundary conditions of the surface currents at the north-east corner of the domain drive the instability and the oscillations depend on the ocean reanalysis adopted. In the CLS region, on the other hand, the model is capable of reproducing a significant portion of the interannual variability (Fig. 9c), despite underestimating the

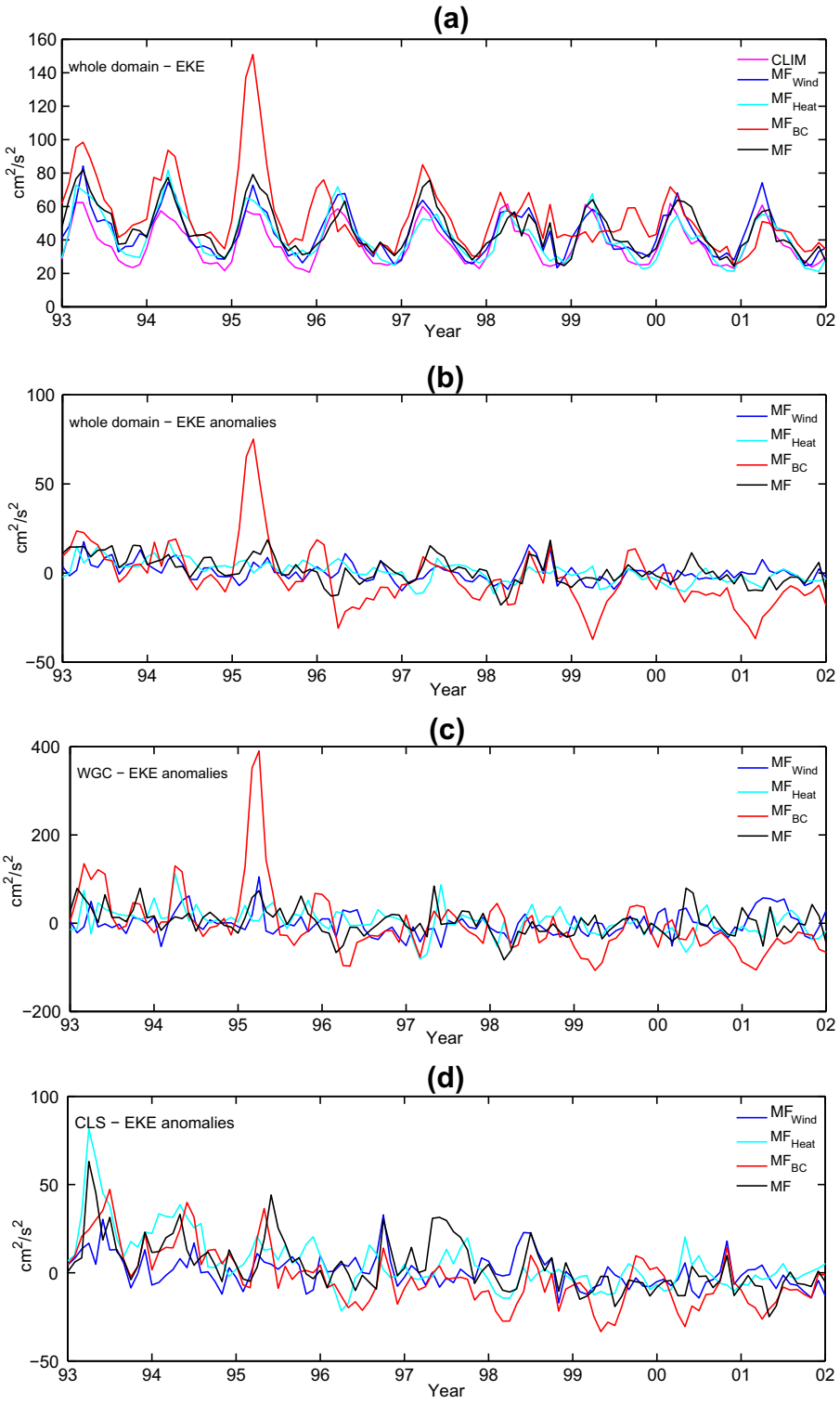


**Fig. 8.** (a) 1993–2001 time-series of monthly eddy kinetic energy (EKE) averaged over the whole domain. (b) As in (a) but after removing the seasonal cycle. (c) Monthly EKE anomalies averaged over the West Greenland Current (WGC) domain. (d) Monthly EKE anomalies averaged over Central Labrador Sea (CLS) domain. CLIM (magenta, 9 years within the 50-years integration) is shown only in panel (a); in (a)–(d) MF (black, one ensemble member), $MF_{Wind}$ (blue), $MF_{Heat}$ (light blue) and $MF_{BC}$ (red, one member) experiments are displayed. (For interpretation of the references to colour in this figure legend, the reader is referred to the web version of this article.)

number of eddies that penetrate from the WGC box. After removing the seasonal cycle, the observed and model EKE anomaly time-series appear to be 99% statistically significantly correlated over the period 1993–2001. The correlation coefficients of the monthly anomaly time-series are $cc = 0.49 \pm 0.02$ for MF and $cc = 0.38 \pm 0.04$, for $MF_{BC}$. Using a 5-month low-pass filter, the correlations reach $0.55 \pm 0.03$ and $0.47 \pm 0.05$, for MF and $MF_{BC}$, respectively, and their significance is 95% according to a *t*-test. If the seasonal cycle is retained the month-to-month correlation between model runs and observations exceeds 0.8 in all cases. The model time-series displays a low frequency modulation at decadal scales with minimum activity in the early '80, between 1985 and

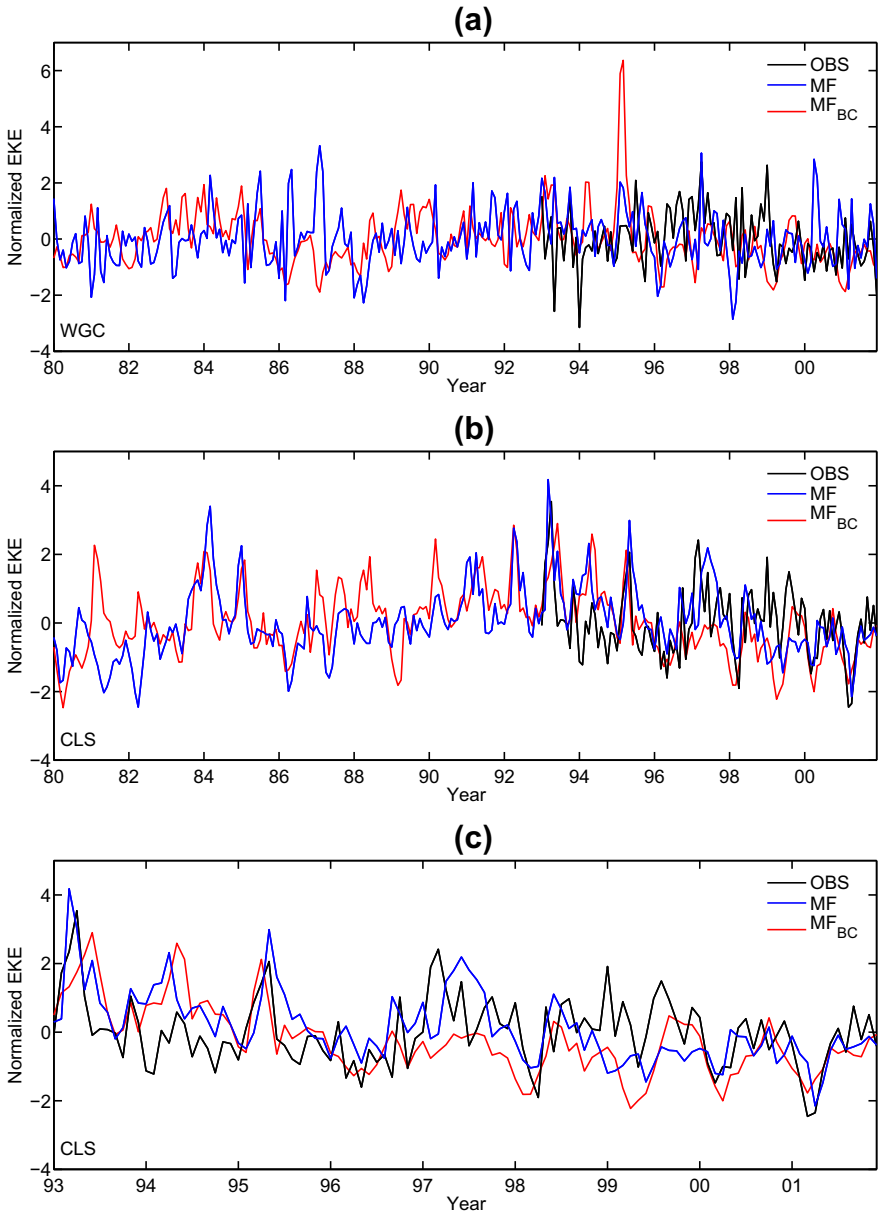


**Fig. 9.** Time-series of monthly EKE anomalies for one member of the MF (blue) and $MF_{BC}$ (red) integrations over the period 1980–2001 and for altimeter observations (black, from Brandt et al. (2004)) over the period 1993–2001 in the WGC (panel a) and CLS (panel b) regions. Panel c shows a zoom on the 1993–2001 period in the CLS area. (For interpretation of the references to colour in this figure legend, the reader is referred to the web version of this article.)

1989 and from 1998 onward and maxima around 1984 and 1993 (Fig. 9b).

It is quite surprising to reproduce such a percentage of the observed variance with a regional model, considering the intrinsic difficulties in simulating the Labrador Sea domain and the model errors, the limited spatial and temporal resolution in the atmospheric forcing fields, the uncertainties in the atmospheric reanalysis and in the oceanic boundary conditions at those latitudes, and the relative high signal-to-noise ratio in the satellite data over the CLS box.

Further investigating the role of the atmospheric forcing, an important question to answer if whether the NAO and/or the AO indices modulate the interannual component of the Labrador Sea EKE, as suggested, between others, by Brandt et al. (2004), Pickart et al. (2002), and Lazier et al. (2002). The NAO index represents the dominant mode of interannual variability over the North Atlantic and consists of a north–south dipole of anomalies, with one center located over Greenland and the other, of opposite sign, over the central latitudes of the North Atlantic and its calculation is based on Rotated Principal Component Analysis (RPCA) applied to monthly standardized 500-mb height anomalies between 20° and 90°N. The AO index, on the other hand, is defined as the first EOF of the monthly mean 1000-hPa height anomalies poleward of 20° latitude for the Northern Hemisphere, has a loading pattern centered in the Arctic and quantifies the modulation in strength of the polar vortex. The indices used in this work are monthly anomalies provided by the Climate Prediction Center at NOAA.[2] The NAO

[2] The NAO and AO indices are available respectively at http://www.cpc.noaa.gov/products/precip/CWlink/pna/norm.nao.monthly.b5001.current.ascii.table and http://www.cpc.noaa.gov/products/precip/CWlink/daily_ao_index/monthly.ao.index.b50.current.ascii. A full description of the methodology used to derive them is presented at http://www.cpc.ncep.noaa.gov/products/precip/CWlink/daily_ao_index/history/method.shtml.

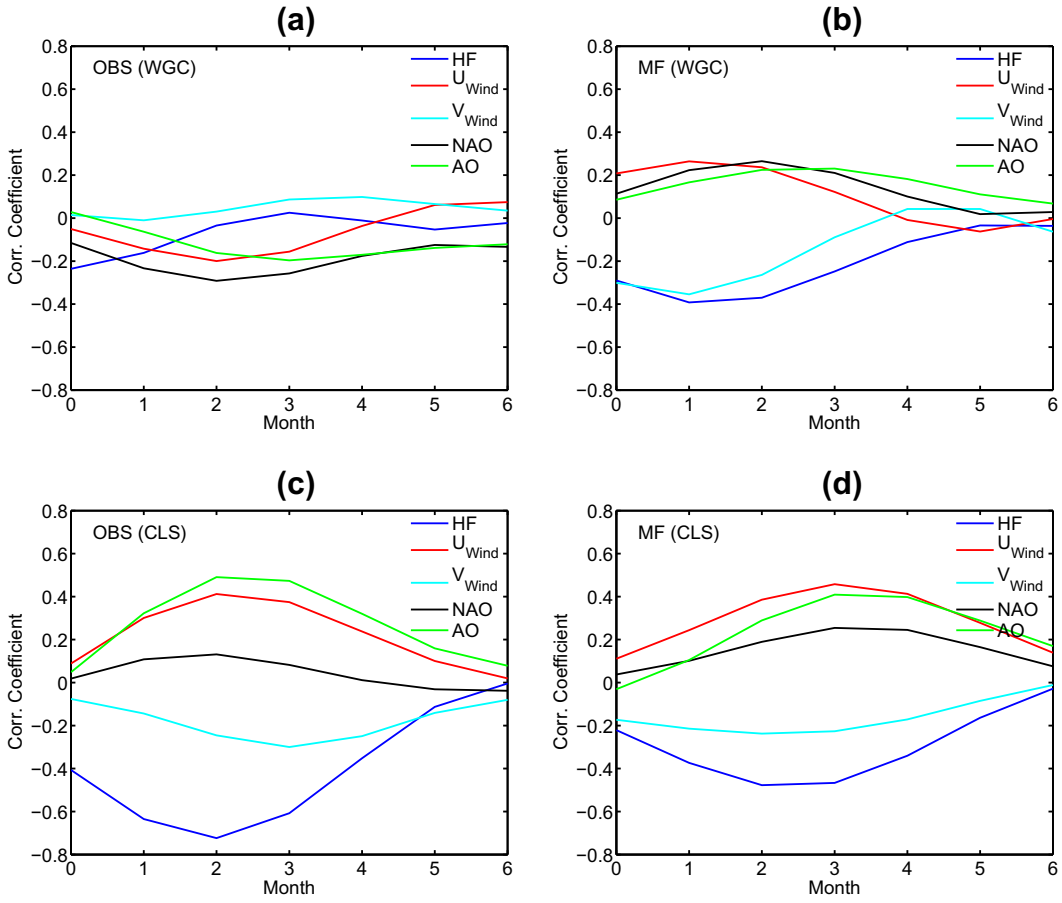


**Fig. 10.** Lag correlation coefficients between the monthly EKE anomalies and leading local heat fluxes (blue), zonal wind component (red), meridional wind component (light blue), NAO index (black) and AO index (green), for (a) satellite observations over 1993–2001 and (b) the MF model ensemble over 1980–2001 in the WGC region; (c) satellite observations and (d) the MF integrations in the CLS area. (For interpretation of the references to colour in this figure legend, the reader is referred to the web version of this article.)

and AO indices are similar but not identical (Ambaum et al., 2001). Their correlation, on a monthly base and over both 1980–2001 and 1993–2001 periods, is 0.58. It does not change significantly if a 5-month running mean is implemented ($cc = 0.57$), indicating that the interannual variability of the two indices shares indeed only part of the variance. A higher correlation is found when considering seasonal averages for winter only ($cc = 0.7$ for the November to February season), while differences between the two indices are more evident in summer ($cc = 0.53$ for the July to October season). From the results presented so far in the model experiments remote atmospheric teleconnections can be expected to drive part of the interannual variability in the CLS region. In Fig. 10, we show the lag correlation curves between the EKE anomaly time-series and the remote atmospheric forcing (NAO/AO indices) or the local atmospheric forcing anomalies (heat fluxes and meridional and zonal components of the wind field) for the satellite data and the MF ensemble. Lag correlations are calculated over 1993–2001 for the satellite observations (Brandt et al., 2004) and over the 1980–2001 period for the model data. All time-series used to calculate the correlations have been smoothed with a 5-month running mean. In the WGC box no statistically significant correlations are found at any lag in the observations (Fig. 10a). This is confirmed in the $MF_{BC}$ integrations (not shown), where the surface current is the main driver of intraseasonal and interannual variations. In the MF ensemble, on the other hand, zonal winds can be used as precursors to explain about 20% of the variance of the EKE anomalies. This is due to the climatological boundary conditions and the consequent lack of interannual variability in the current system along Greenland (Fig. 10b). In the CLS region the maximum correlation between local heat fluxes and zonal wind anomalies and EKE anomalies is found for the atmospheric forcing preceding the EKE response by 2 months in the observations and 3 months in the model, respectively. Local heat fluxes are the best predictor for the EKE variations in both observations and numerical integrations, with a correlation reaching an impressive $cc = -0.72$ for NCEP heat fluxes leading the eddy kinetic energy anomalies in the satellite record by 2 months. In the model runs the wind vector field contributes to the surface EKE variability more than the heat fluxes, as seen by comparing $MF_{Wind}$ and $MF_{Heat}$, but when its components or intensity are singled out, their respective predictor skills are lower. No statistical significant correlations are found in the model or in the observations between EKE anomalies and the NAO index. Therefore the NAO cannot be used as forecasting tool on a yearly base for EKE variations, even if its low frequency component shares common features with the EKE variability on decadal scales. A higher skill, barely statistically significant in the model but reaching $cc = 0.49$ (thus explaining about 25% of the total variance) in the observations, is achieved when using the AO index, which is directly linked to the modulation of the circumpolar flow (Ambaum et al., 2001), suggesting a substantial contribution of the Arctic to the Labrador Sea variability. In particular in the CLS region the AO index is better correlated with the local heat fluxes than the NAO, with $cc = -0.58$ ($-0.58$) for the AO and $cc = -0.47$ ($-0.46$) for the NAO using monthly (5-month running mean) anomalies, while analogous correlations are found between the zonal and meridional wind components

and the two climatic indices. In the model at decadal scales the AO index low-pass filtered at 5 years reproduces the modeled EKE changes better than the NAO, but the low number of degrees of freedom does not allow to validate the significance of this result. Analogous conclusions are reached for $MF_{BC}$ runs with slightly lower correlations (about 10% – not shown).

Finally, we show that the atmospheric forcing drives the EKE interannual variability in the CLS region in both the model and the satellite observations with a simple first-order auto-regressive (AR1) model in which the rate of change of the surface EKE in the MF run integrates the atmospheric variability associated with local NCEP heat fluxes $HF_{NCEP}$ according to:

$$\frac{dEKE_{AR1}}{dt} = \alpha HF_{NCEP}(t) - \frac{EKE_{AR1}(t)}{\tau}. \quad (4)$$

The ocean memory to the heat fluxes perturbations is represented in the damping term (second term on the right-hand side). The timescale of the damping $\tau$ is computed from the auto-decorrelation timescale of the monthly EKE time-series and it is equal to 3 months in the model. $\alpha$ is a normalization coefficient. The correlation between the model monthly EKE anomalies and $EKE_{AR1}$ is $cc = 0.5$. The same AR1 model fits the satellite data with a correlation coefficient $cc = 0.68$ (Fig. 11). The significance of the correlation coefficients is estimated with a Monte Carlo test from the Probability Distribution Functions (PDFs) of the correlation coefficient of two red-noise time-series with the same autoregression coefficients of the original signals. The PDFs are computed by generating 10,000 realizations of the red-noise time-series. If the zonal wind component is used to construct the AR1 model in addition to the heat fluxes, results do not improve significantly; if used instead of $HF_{NCEP}$ the performance of the AR1 deteriorates slightly. This supports the simple model proposed by Halliwell and Mayer (1996) and their conclusion that in the North Atlantic wind induced heat fluxes anomalies are integrated by the mixed-layer and represent the first-order contributor to the mixed-layer balance.

Our results, all taken together, suggest that in the Central Labrador Sea the AO modifies the zonal winds that in turn lead to local anomalies in the heat fluxes. Those anomalies, integrated by the ocean, contribute to the generation of eddies that populate the CLS region.

## 5. Discussion and conclusions

We compared ensemble numerical simulations of the Labrador Sea circulation performed with a regional ocean model, ROMS, over the period 1980–2001 with different forcings and boundary conditions. The interactions between the atmospheric and oceanic circulations in the Labrador Sea basin are represented with increased degree of complexity. The main goal of this work is to identify, for the first time in a modeling framework, the physical processes regulating the interannual variability of the surface eddy kinetic energy variability in this area.

In all integrations the eddy kinetic energy field is characterized by a maximum extending from the West coast of Greenland towards the interior and localized around 61° – 62°N. The eddies are formed at a higher rate in winter and spring and have a diameter of about 35–40 km. The eddies are mainly anticyclonic and are generated by baroclinic instability of the flow passing over an abrupt change in the topographic slope south of Cape Desolation, as shown already by previous studies (Eden and Böning, 2002; Bracco and Pedlosky, 2003; Katsman et al., 2004; Bracco et al., 2008).

In a first two-member ensemble the regional ocean model is forced by monthly varying atmospheric heat and momentum fluxes and by climatological oceanic boundary conditions (MF). The variability of the intense eddy shedding in correspondence of

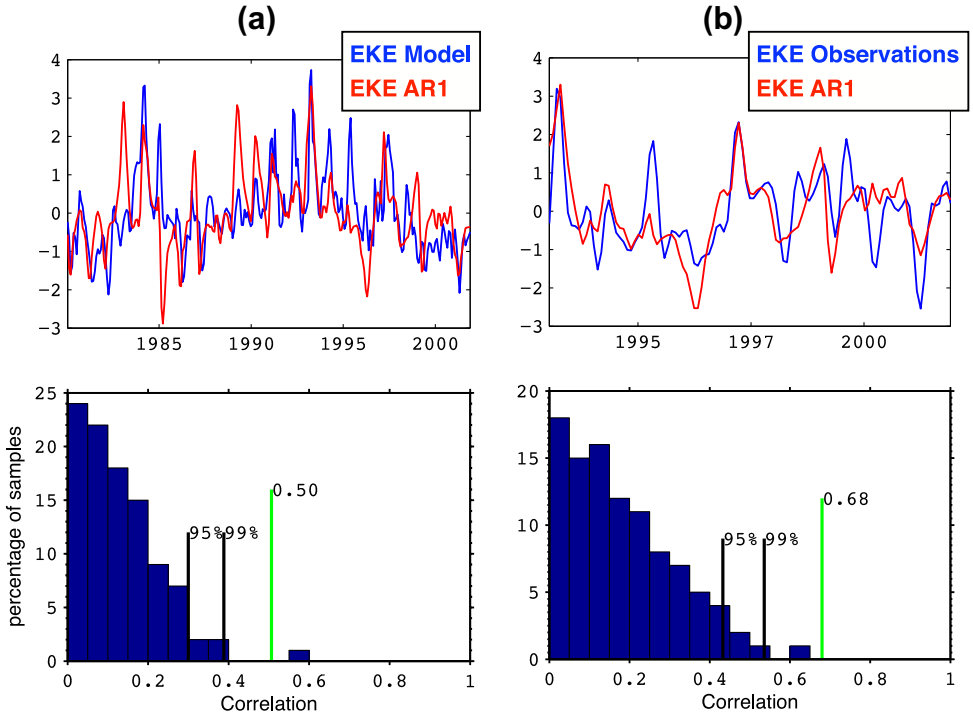


**Fig. 11.** Top: The model (a) and observed (b) monthly EKE anomalies in the CLS region (blue) and the reconstructed ones using a AR1 model forced by a time-series of heat fluxes from NCEP/NCAR reanalysis (red). Units are in standard deviations (std). Bottom: The significance of correlation of the monthly values ($cc = 0.50$ in the model and $cc = 0.68$ for the satellite record, both >99% significant) estimated using a Monte Carlo test for time-series with a red spectra and the same autoregression coefficients of the original signals. (For interpretation of the references to colour in this figure legend, the reader is referred to the web version of this article.)

the EKE maximum along the coast of Greenland is driven at interannual scales by the strength of the bottom boundary current, while the seasonal cycle is dictated by the local atmospheric forcing. The ocean variability internal to the Labrador Sea domain is responsible for the intrinsic changes in the bottom current and the predictability in this area is therefore limited. In the Central Labrador Sea (CLS region), on the other hand, the local atmospheric forcing drives a significant portion of the interannual EKE variability and eddies formed at the EKE maximum in the WGC region are not instrumental to explain those interannual changes.

In a second ensemble the regional ocean open boundaries are forced by monthly varying incoming currents derived from SODA ($MF_{BC}$). In $MF_{BC}$ the highly variable surface component of the East Greenland current modulates the variance in the modeled EKE maximum north of Cape Desolation. When comparing the eddy field in the WGC area in the two ensembles, we find that the eddies extend through the whole water column in both cases, but they are more intense and longer living in the $MF_{BC}$ than in MF integrations. In all runs, though, ROMS is unable to reproduce the observed rate of southward migration and the 1–2 year long lifespan of the eddies. Therefore fewer than observed eddies move as south as 58°N and modeled eddies keep their coherence for less than 1 year.

The East Greenland current that drives the interannual variability of the Irminger Rings shedding in the $MF_{BC}$ ensemble directly connects the Arctic to the Northern Atlantic and it is a major contributor to sea ice export out of the Arctic. Its variability is linked to the state of the subpolar gyre and to the fresh water input from the Arctic, and its representation in ocean reanalysis – like SODA – or models is poor, due to the intrinsic difficulties of including all those processes and to the paucity of detailed observations for data assimilation exercises. Indeed a comparison of three reanalysis datasets has shown little agreement, mining the reliability of our month-by-month representation of the WGC interannual variability. Nonetheless, our integrations indicate that the variability in the vertical shear that drives the eddy formation by baroclinic instability in the WGC region is linked to the varying strength of the surface current, and not to the atmospheric forcing. This conclusion is likely to hold in the 'real' ocean, as suggested by the nonsignificant correlations between the atmospheric forcing fields and the observed surface EKE in this area. The details of the modeled interannual variability in the WGC region, however, depend on the particular reanalysis chosen, and cannot be successfully compared to the observations.

In the center of the domain, on the other hand, the monthly varying boundary conditions do not impact significantly the dynamics, and local atmospheric forcing drives a substantial component of the interannual and intraseasonal variability. The link between local atmospheric forcing and EKE is confirmed in the analysis of a 9-year long satellite record over the common period January 1993–December 2001. This analysis suggests that the Irminger rings observed to propagate in the CLS region, whose characteristics are not completely captured in our integrations, do not represent the only source of surface variability in the center of the basin. The Central Labrador Sea is capable of generating its own eddies, mainly anticyclonic and of smaller diameter than Irminger Rings (see movie of surface vorticity in Supplementary material) in response to sensible and latent heat losses in spring and fall, when the mixed layer is deeper. In the model the averaged mixed layer depth required for eddy formation is about 100 m. Further studies with higher vertical resolution and better representation of mixed-layer mixing are required to investigate the existence of a mixed-later depth threshold for eddy generation and possibly convective activity.

In both the observations and our integrations heat fluxes – and to a lesser extent zonal winds – can be used as predictors of the surface EKE anomalies in the Central Labrador Sea, where deep convection occurs, with a lead of 2–3 months. The Arctic Oscillation index, that implicitly contains information about the zonal wind field and heat fluxes over the basin, can also provide useful indications and broadly varies in synchrony with the EKE in the central part of the Labrador Sea, while the North Atlantic Oscillation index does not quantify the local changes in the atmospheric forcing fields with the same accuracy.

Finally, we have been able to reproduce with good statistical confidence the modeled EKE variability in the CLS region with a simple AR1 model in which the local heat fluxes force the rate of change of the EKE. The same model, using coefficients derived from our simulations, has been successfully implemented to reproduce the observed interannual variability in the CLS box in the satellite data.

In summary, this work shows that despite the inability of our model to properly simulate the lifespan and the southward propagation of the Irminger Rings, and the uncertainties in the heat flux reanalysis at high latitudes, it is possible to reproduce a substantial portion of the observed EKE variability in the center of the basin, where deep convection occurs. Our results indicate that sensible and latent heat losses integrated over a 2–3 month period and partially controlled by the Arctic Oscillation at a broader scale, regulate the interannual surface EKE variability away from the boundary current systems. It is tantalizing to speculate that if the amount of deep water formation in the Labrador Sea is directly linked to the surface EKE variability, then contrary to expectations the preconditioning by Irminger eddies does not play a major role in modulating deep convection and the atmospheric forcing alone can help predicting onset and strength of convective events. Hints in this direction are contained in the recent analysis of deep convective activities in three consecutive winters by Våge et al. (2009) and Yashayaev and Loder (2009). This would confirm, on a more local scale, the model analysis performed by Delworth and Greatbatch (2000) that suggests that the multidecadal variability of Atlantic Meridional Overturning Circulation is predominately driven by the low-frequency component of surface heat fluxes.

This work may help extrapolating back in time the EKE variability in a region of key climatic importance, where in situ observations are sparse and satellite data are available only from the early 90s', and points to the need for monitoring the East Greenland Current system to better understand and predict the EKE maximum off the West coast of Greenland.

## Acknowledgments

We wish to thank Joe Pedlosky for his valuable suggestions, and Igor Yashayaev and two anonymous reviewers for their insightful comments that helped improving this manuscript. This work is supported entirely through the NSF Grant OCE-0751775.

## Appendix A

Our study domain extends northward from 51°N to 66°N and westward from 35°W to 65°W. The spatial resolution is 7.5 km with 30 levels in the vertical. As mentioned in the paper the model bathymetry ($h$) is derived from ETOPO2 (a 2-Minute Gridded Global Relief Data Collection topography, Sandwell and Smith (1997)). An iterative averaging procedure is applied to prevent under-sampling. Additionally, to reduce the pressure gradient errors typical of $\sigma$ or $s$ coordinate models, the bathymetry is smoothed to reduce the slope parameter $r$ defined as $r = |h_{+1/2} - h_{-1/2}|/|h_{+1/2} + h_{-1/2}| \approx \nabla h/h$. A modified Shapiro smoother is applied iteratively on the logarithmic space to achieve the smoothing procedure. In our

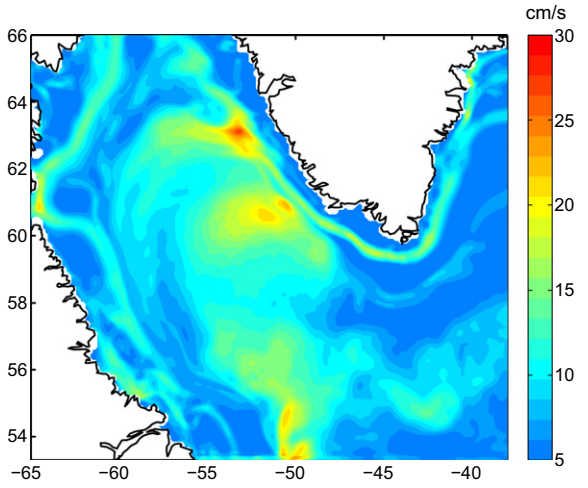


**Fig. A1.** Annual mean distribution of surface EKE cast as a speed $V_{EKE} = (2EKE)^{1/2}$ for an integration where the Shapiro smoother is applied everywhere in the Labrador Sea domain. The baroclinic instability off Cape Desolation is heavily dumped and a secondary peak of the EKE is unrealistically simulated around 63°N where the shallow bathymetry forces the West Greenland Current to detach from the Greenland coastline.

model grid, the maximum slope of the topography $r$ is allowed to be 0.35. However, the topographic details near Cape Desolation control the boundary current meandering and the subsequent shedding of the eddies (Eden and Böning, 2002; Katsman et al., 2004; Bracco et al., 2008). Our experiments show that the modeled circulation is extremely sensitive to the local bathymetry in the West Greenland region (WGC, 60°N–62.5°N, 48°W–52°W). The smoothing procedure in this region can cause the appearance of an unrealistic eddy kinetic energy (EKE) peak further north (around 63°N) compared to the observations (Lilly et al., 2003) (See Fig. A1). To overcome this problem, we adopted an embedded bathymetry: The bathymetry is first interpolated to the model grid and then smoothed over the whole area with the Shapiro filter on $\log(h)$ space. Finally, the original ETOPO2 bathymetry data is replaced along the West Greenland Current region in three boxes with coordinates [52.06°W–50.46°W] [61.76°N–62.52°N]; [51.39°W–49.52°W] [61.00°N–61.76°N]; [50.32°W–48.45°W] [60.01°N–61.00°N]. A linear interpolation is applied to the bathymetry along the boundary nodes of these three boxes. We verified with boxes of different size that the chosen bathymetry system not only minimize the pressure gradient errors arising from steep and tall features, but also retains the details of the topography along the west side of the Greenland necessary to properly simulate the eddy generation induced by the localized baroclinic instability. Fig. A2 shows the baroclinic and barotropic conversion terms averaged only over the top 100–400m of the water column, and displays the underestimation of the baroclinic term when deeper waters are not accounted for in the MF runs.

## Appendix B. Supplementary data

Supplementary data associated with this article can be found, in the online version, at doi:10.1016/j.pocean.2011.01.006.

The movie included in the Supplementary material shows the evolution of the surface relative vorticity field in the Labrador Sea during 1997 and 1998 for the MF integration.

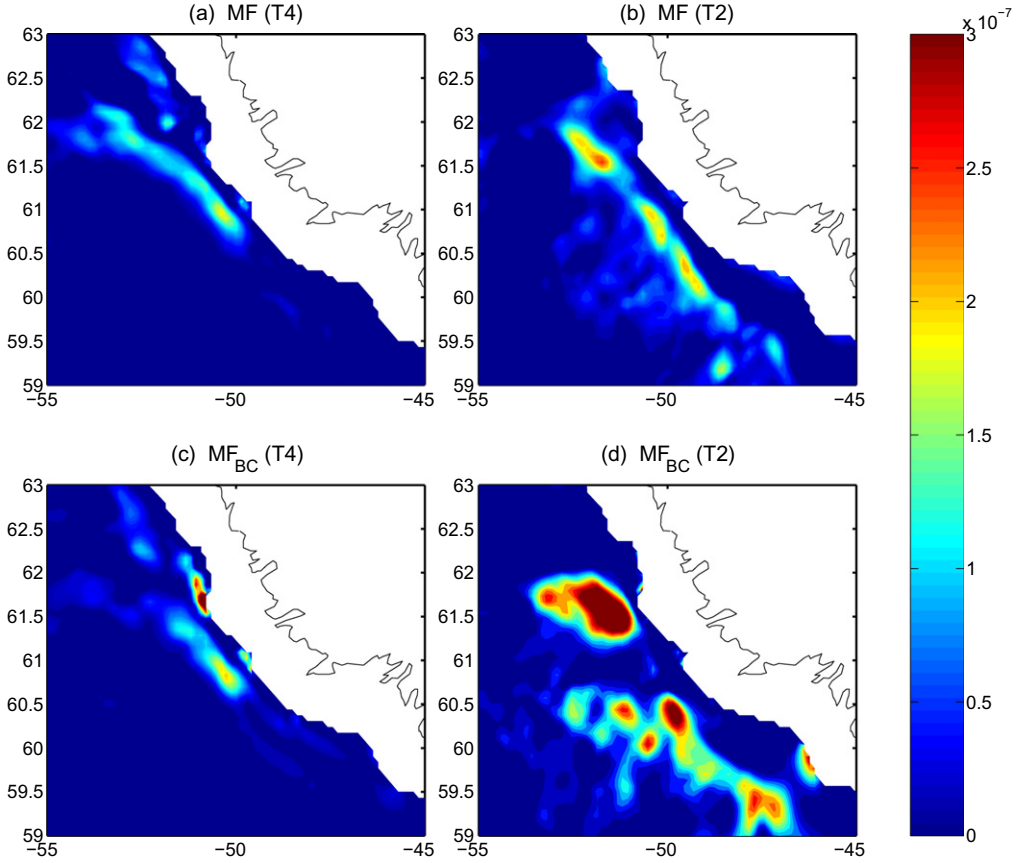


**Fig. A2.** Barotropic ($T_4$, left panels) and baroclinic ($T_2$, right panels) conversion terms vertically averaged over the top 100–400 m of water column following Eden and Böning (2002) for MF (top) and $MF_{BC}$ (bottom), to be compared with Fig. 7.

## References


Ambaum, M.A., Hoskins, B.J., Stepehnson, D.B., 2001. Arctic oscillation or north atlantic oscillation? J. Climate 14, 3495–3507.

Balmaseda, M., Vidard, A., Anderson, D., 2007. The ECMWF System 3 ocean analysis system. ECMWF Technical Memorandum 508.

Beckmann, A., Böning, C.W., Brügge, B., Stammer, D., 1994. On the generation and role of eddy variability in the central North Atlantic Ocean. J. Geophys. Res. 99, 20381–20391.

Bracco, A., LaCasce, J., Pasquero, C., Provenzale, A., 2000. Velocity pdfs in barotropic turbulence. Phys. Fluids 12, 2478–2488.

Bracco, A., Pedlosky, J., 2003. Vortex generation by topography in locally unstable baroclinic flows. J. Phys. Oceanogr. 33, 207–219.

Bracco, A., Pedlosky, J., Pickart, R.S., 2008. Eddy formation near the west coast of Greenland. J. Phys. Oceanogr. 38, 1992–2002.

Brandt, P., Schott, F.A., Funk, A., Martins, C.S., 2004. Seasonal to interannual variability of the eddy field in the Labrador Sea from satellite altimetry. J. Geophys. Res. 109, C02028.

Carton, J.A., Giese, B.S., 2008. A reanalysis of ocean climate using SODA. Mon. Wea. Rev. 136, 2999–3017.

Cayan, D.A., 1992. Latent and sensible heat flux anomalies over the northern oceans: driving the sea surface temperatures. J. Phys. Oceanogr. 22, 859–881.

Chanut, J., Barnier, B., Large, W., Debreu, L., Penduff, T., Molines, J.M., Mathiot, P., 2008. Mesoscale eddies in the Labrador Sea and their contribution to convection and re-stratification. J. Phys. Oceanogr. 38, 1617–1643.

Combes, V., Lorenzo, E.D., 2007. Intrinsic and forced interannual variability of the Gulf of Alaska mesoscale circulation. Prog. Oceanogr. 75, 266–286.

Cuny, J., Rhines, P.B., Niiler, P.P., Bacon, S., 2002. Labrador Sea boundary currents and the fate of the Irminger Sea Water. J. Phys. Oceanogr. 32, 627–647.

Delworth, T.L., Greatbatch, R.J., 2000. Multidecadal thermohaline circulation variability driven by atmospheric surface flux forcing. J. Climate 13, 1481–1495.

Dickson, R., Lazier, J., Meincke, J., Rhines, P., Swift, J., 1996. Long-term coordinated changes in the convective activity of the North Atlantic. Prog. Oceanogr. 38, 241–295.

Eden, C., Böning, C., 2002. Sources of eddy kinetic energy in the Labrador Sea. J. Phys. Oceanogr. 32, 3346–3363.

Fisher, J., Schott, F., Dengler, M., 2004. Boundary circulation at the exit of the Labrador Sea. J. Phys. Oceanogr. 34, 1548–1570.

Flierl, G.R., Pedlosky, J., 2007. The nonlinear dynamics of time-dependent subcritical baroclinic currents. J. Phys. Oceanogr. 37, 1001–1021.

Haidvogel, D.B., Arango, H., Hedstrom, K., Beckmann, A., Malanotte-Rizzoli, P., hchepetkin, A.S., 2000. Model evaluation experiments in the North Atlantic basin: simulations in nonlinear terrain-following coordinates. Dyn. Atmos. Oceans 32, 239–281.

Halliwell, G.R., Mayer, D.A., 1996. Frequency response properties of forced climatic SST anomaly variability in the North Atlantic. J. Climate 9, 3575–3587.

Hátún, H., Eriksen, C.C., Rhines, P.B., 2007. Buoyant eddies entering the Labrador Sea observed with gliders and altimetry. J. Phys. Oceanogr. 37, 2838–2854.

Hátún, H., Sandø, A., Drange, H., Hansen, B., Valdimarsson, H., 2005. Influence of the Atlantic subpolar gyre on the thermocline circulation. Science 309, 1841–1844.

Jones, H., Marshall, J., 1997. Restratification after deep convection. J. Phys. Oceanogr. 27, 2276–2287.

Josey, S.A., 2001. A comparison of ECMWF, NCEP NCAR, and SOC surface heat fluxes with moored buoy measurements in the subduction region of the Northeast Atlantic. J. Climate 14, 1780–1789.

Kalnay, E., Kanamitsu, M., Kistler, R., Collins, W., Deaven, D., Gandin, L., Iredell, M., Saha, S., White, G., Woollen, J., Zhu, Y., Chelliah, M., Ebisuzaki, W., Higgins, W., Janowiak, J., Mo, C., Ropelewski, C., Wang, J., Leetmaa, A., Reynolds, R., Jenne, R., Joseph, D., 1996. The NCEP/NCAR 40-year reanalysis project. Bull. Am. Meteorol. Soc. 77, 431–437.

Katsman, C., Spall, M., Pickart, R.S., 2004. Boundary current eddies and their role in the restratification of the Labrador Sea. J. Phys. Oceanogr. 34, 1967–1983.

Kushnir, Y., 1994. Interdecadal variations in the North Atlantic sea surface temperatures and associated atmospheric conditions. J. Climate 7, 141–157.

Large, W.G., Mc Williams, J.C., Doney, S., 1994. Oceanic vertical mixing: a review and a model with a non-local K-profile boundary layer parameterization. Rev. Geophys. 32 (4), 363–403.

Lavender, K.L., Davis, R.E., Owens, W.B., 2000. Mid-depth recirculation observed in the interior Labrador and Irminger seas by direct velocity measurements. Nature 407, 66–69.

Lazier, J., Hendry, R., Clarke, A., Yashayaev, I., Rhines, P., 2002. Convection and restratification in the Labrador Sea, 1990–2000. Deep-Sea Res. Pt. I 49, 1819–1835.

Lilly, J.M., Rhines, P.B., Schott, F., Lavender, K., Lazier, J., Send, U., D'Asaro, E., 2003. Observations of the Labrador Sea eddy field. Prog. Oceanogr. 59, 75–176.

Malanotte-Rizzoli, P., Hedstrom, K., Arango, H., Haidvogel, D., 2000. Water mass pathways between the subtropical and tropical ocean in a climatological simulation of the North Atlantic ocean circulation. Dyn. Atmos. Oceans 32, 331–371.

Marchesiello, P., Mc Williams, J.C., Shchepetkin, A., 2001. Open boundary conditions for long-term integration of regional oceanic models. Ocean Modell. 3, 1–20.

Marshall, J., Schott, F., 1999. Open-ocean convection: observations, theory and models. Rev. Geophys. 37, 1–64.

Masuda, S., Awaji, T., Toyoda, T., Shikana, Y., Ishikawa, Y., 2009. Temporal evolution of the equatorial thermocline associated with the 1991–2006 ENSO. J. Geophys. Res. 114, C03015.

Mellor, G.L., Ezer, T., Oey, L.Y., 1994. The pressure gradient conundrum of sigma coordinate ocean models. J. Atmos. Ocean Tech. 11, 1126–1134.

Penduff, T., Barnier, B., Dewar, W.K., O'Brien, J.J., 2004. Dynamical response of the oceanic eddy field to the North Atlantic Oscillation: a model–data comparison. J. Phys. Oceanogr. 34, 2615–2629.

Penven, P., Marchesiello, P., Debreu, L., Lefevre, J., 2008. Software tools for pre- and post-processing of oceanic regional simulations. Environ. Model. Softw. 23, 660–662.

Petersen, M.R., Julien, K., Weiss, J.B., 2006. Vortex cores, strain cells, and filaments in quasigeostrophic turbulence. Phys. Fluids 18, 026601.

Pickart, R.S., Spall, M.A., Spall, M.A., Ribergaard, M.H., Moore, G.W.K., Milliff, R.F., 2003. Deep convection in the Irminger Sea forced by the Greenland tip jet. Nature 424, 152–156.

Pickart, R.S., Torres, D.J., Clarke, R.A., 2002. Hydrography of the Labrador Sea during active convection. J. Phys. Oceanogr. 32, 428–457.

Prater, M.D., 2002. Eddies in the Labrador Sea as observed by profiling RAFOS floats and remote sensing. J. Phys. Oceanogr. 32, 411–427.

Reynaud, T.H., Weaver, A.J., Greatbatch, R.J., 1995. Summer mean circulation of the northwestern Atlantic Ocean. J. Geophys. Res. 100, 779–816.

Rykova, T., Straneo, F., Lilly, J.M., Yashayaev, I., 2009. Irminger current anticyclones in the Labrador Sea observed in the hydrographic record, 1990–2004. J. Mar. Res. 67, 361–384.

Sandwell, D.T., Smith, W., 1997. Marine gravity anomaly from Geosat and ERS-1 satellite altimetry. J. Geophys. Res. 102, 10039–10054.

Shchepetkin, A., Mc Williams, J.C., 2003. A method for computing horizontal pressure-gradient force in an oceanic model with a nonaligned vertical coordinate. J. Geophys. Res. 108, 35.1–35.34.

Shchepetkin, A., Mc Williams, J.C., 2005. The regional oceanic modelling system (ROMS): a split-explicit, free-surface, topography-following-coordinate oceanic model. Ocean Modell. 9, 347–3404.

Smith, T.M., Reynolds, R.W., 2004. Extended reconstruction of global sea surface temperatures based on COADS data (1854–1997). J. Climate 17, 2466–2477.

Song, Y., Haidvogel, D., 1994. A semi-implicit ocean circulation model using a generalized topography-following coordinate system. J. Comput. Phys. 115, 228–244.

Spall, M., 2004. Buoyancy-forced circulations in shallow marginal seas. J. Phys. Oceanogr. 34, 1197–1213.

Straneo, F., 2006. On the connection between dense water formation, overturning, and poleward heat transport in a convective basin. J. Phys. Oceanogr. 36, 1822–1840.

Talley, L.D., McCartney, M.S., 1982. The distribution and circulation of Labrador Sea Water. J. Phys. Oceanogr. 12, 1189–1205.

Thompson, D.W., Wallace, J.M., 1998. The Arctic Oscillation signature in the wintertime geopotential height and temperature fields. Geophys. Res. Lett. 25, 1297–1300.

Treguier, A.M., Theetten, S., Chassignet, E.P., Penduff, T., Smith, R., Talley, L., Beismann, J.O., Böning, C., 2005. The North Atlantic subpolar gyre in four high-resolution models. J. Phys. Oceanogr. 35, 757–774.

Våge, K., Pickart, R.S., Moore, G.W.K., Ribergaard, M.H., 2008. Winter mixed-layer development in the central Irminger Sea: the effect of strong, intermittent wind events. J. Phys. Oceanogr. 38, 541–565.

Våge, K., Pickart, R.S., Thierry, V., Reverdin, G., Lee, C.M., Petrie, B., Agnew, T.A., Wong, A., Ribergaard, M.H., 2009. Surprising return of deep convection to the subpolar North Atlantic Ocean in winter 2007–2008. Nat. Geosci. 2, 67–72.

Weiss, J., 1981. The dynamics of enstrophy transfer in two-dimensional turbulence. Physica D 48, 273–294.

Wolfe, C.L., Cenedese, C., 2006. Laboratory experiments on eddy generation by a buoyant coastal current flowing over variable bathymetry. J. Phys. Oceanogr. 36, 395–411.

Yashayaev, I., 2007. Hydrographic changes in the Labrador Sea, 1960–2005. Prog. Oceanogr. 73, 242–276.

Yashayaev, I., Loder, J.W., 2009. Enhanced production of Labrador Sea Water in 2008. Geophys. Res. Lett. 36, L01606.